Chapter 8. Microwave Sea Ice Signature Modeling

DALE P. WINEBRENNER
Polar Science Center, Applied Physics Laboratory, University of Washington, 1013 NE 40th Street, Seattle, Washington 98105

JONATHAN BREDOW AND ADRIAN K. FUNG
University of Texas, P. O. Box 19016, Arlington, Texas 76019

MARK R. DRINKWATER AND SON NGHIEM
Jet Propulsion Laboratory, California Institute of Technology, 4800 Oak Grove Drive, Pasadena, California 91109

ANTHONY J. GOW AND DONALD K. PEROVICH
Cold Regions Research and Engineering Laboratory, 72 Lyme Road, Hanover, New Hampshire 03755–1290

THOMAS C. GRENFELL
Department of Atmospheric Sciences, University of Washington, Seattle, Washington 98195

HSIU C. HAN AND JIN A. KONG
Massachusetts Institute of Technology, Cambridge, Massachusetts 02139

JAY K. LEE
Department of Electrical and Computer Engineering, Syracuse University, 121 Link Hall, Syracuse, New York 13244-1240

SABA MUDALIAR
Hanscom Air Force Base, Massachusetts 01731

ROBERT G. ONSTOTT
Environmental Research Institute of Michigan, P. O. Box 8618, Ann Arbor, Michigan 48107

LEUNG TSANG AND RICHARD D. WEST
Department of Electrical Engineering, University of Washington, Seattle, Washington 98195

8.1 INTRODUCTION

Remote sensing hinges on the interpretation of signatures and signature changes in terms of geophysical variables. To date, operational microwave remote sensing of sea ice has been based primarily on empirical relations between signatures and ice type or ice type concentrations. Empirical remote sensing has proven valuable in many geophysical studies, but a reliance on empiricism alone severely limits realization of the potential value of remote sensing methods.

Plots of ice signature data versus geophysical parameters often show considerable scatter. Some scatter is due to fundamental limitations in our instruments (e.g., Synthetic Aperture Radar [SAR] speckle), and some is almost surely due to random variations in ice or snow properties with little or no relation to geophysically significant parameters. However, there is evidence that much of what we perceive as scatter is, in fact, caused by variations in interesting geophysical parameters. For example, signatures from ice typically labeled as first-year are variable partly because of an evolution in thin, first-year ice (i.e., nilas and gray ice) signatures as a function of thickness and perhaps other variables. This signature evolution can cause nilas and gray ice to appear brighter than both calm, open water and thicker ice in SAR images (Chapters 5, 14, and 25), and appear to passive microwave algorithms as mixtures of thick first-year and old ice (Chapter 14). Thus, these variations may contain thickness information. As a second example, variations in ice temperature, wind speed (over open water), and atmospheric water content cause variations in passive microwave signatures that look like noise in averaged data, but are at least partly invertible (Chapter 10). Thus, sea ice microwave signatures contain more geophysical information than is routinely utilized;

Microwave Remote Sensing of Sea Ice
Geophysical Monograph 68

much of the potential of sea ice microwave remote sensing remains untapped.

Realizing this potential requires an approach using both observations and physical insight. Ice morphology and properties are highly diverse, even within well-defined, traditional ice types. Signature variations of potential interest (passive or active, variations versus frequency, polarization, and so on) are legion. Thus, to find any but the most obvious links between signatures and geophysical properties, a purely empirical approach would require a huge (and hugely expensive) comprehensive data set, or risk missing valuable links. An exhaustive data set would surely contain much extraneous information, but there is no empirical way to predict which parts would later prove inessential. Moreover, recognizing valuable new links in such a thicket of data would be very difficult. More than a purely empirical approach is needed if we are to find and exploit valuable, but less than obvious, remote sensing opportunities.

Physical understanding and insight offer us the means to interpret data, uncover key regularities, and direct further efforts intelligently. Even a rough understanding of the physics underlying observations can lead to fruitful exploratory organizations of data and new insight. For example, Grenfell [1992] organized noisy passive microwave gradient ratios for old ice by plotting them against an approximate optical depth for the bubbly upper ice layer. The regularity he found suggests that, in addition to more precise work on this link, we investigate links between optical depth and more traditional geophysical parameters, such as ice freeboard.

Building a framework of physical understanding requires quantitative signature modeling and model testing. Several differing qualitative explanations for a given observation may be plausible; the difference in their implications for our understanding and for remote sensing may be considerable. Quantitative comparisons of differing explanations, i.e., models, against data provide a much sharper razor for separating the explanation closest to reality from the rest. The result is a stronger and broader framework of understanding that we can use to guide the next steps of investigation. This dialectic between theory and experiment is fundamental in all areas of physics, both basic and applied.

We derive several collateral benefits from physical understanding and signature models as well. Models allow us to simulate signature data for remote sensing system design, quantifying benefits and costs for various choices of system parameters. Recognizing the limits of our present understanding allows us to better identify situations in which present remote sensing techniques may fail. Thus progress in remote sensing depends on the development and judicious application of quantitative models for signatures.

Research over the past decade has produced a broad but imprecise understanding of the major physical effects determining sea ice signatures, as well as a number of sophisticated microwave signature models for application to sea ice. Microwave sea ice signatures are largely the product of scattering within the ice (volume scattering) and from its interfaces (rough surface scattering), and of interactions between these two types of scattering. A number of models focus on volume scattering to the exclusion of surface scattering, or vice versa; a few models treat both processes but make simplifying assumptions about interactions between the two. All these models are of course founded on Maxwell's equations of classical electrodynamics, and all assume linear, nonmagnetic dielectric behavior of the constituent materials of sea ice. The differences between models arise out of their significantly different sets of approximations, physical descriptions of the scattering material, and emphases on particular aspects of the problem at the expense of others. The highly developed crop of new models has brought us an array of choices in modeling the signature of any particular type of ice.

However, for any given combination of ice type and conditions, not all of the available choices can be appropriate. Many significant questions remain controversial. To give just one example, we have several models for volume scattering in first-year ice, but no generally accepted answer to the question: What is the role of volume scattering in cold first-year ice signatures, relative to surface scattering or other effects, as a function of ice thickness, snow cover, and radiation wavelength? Such questions remain because model development has outpaced model testing. The majority of sea ice model-data comparisons in the literature consist of reasonable-looking model fits to signature observations from ice for which there was little characterization. (Reasons for this include the dependence of scattering models on ice and snow parameters quite different from those measured in geophysical studies, as well as a lack of understanding of needed accuracies in ground truth data.) The problem is that most models contain several tunable parameters and the range of observations that can be fitted is large. Therefore, success with model fitting is, at best, limited evidence for validity of the model under consideration. On the other hand, a model can be excluded via this approach only when no plausible input parameter values produce results similar to observations. A finer criterion is needed to distinguish between competing explanations for the same observations.

That finer criterion is quantitative comparison of signature observations from a given scene with model results based on independent characterization of that same scene. Studies based on such comparisons, notably those by Ulander et al. [1992], Davis et al. [1987], Reber et al. [1987], Stogryn [1987], and Lin et al. [1988], are thus especially valuable (though the latter two works treat only microwave extinction rather than signatures per se, and those by Davis et al. and Reber et al. treat terrestrial snow pack rather than sea ice). However, the body of such work in the literature is far from sufficient. The net result of this situation is that, even as of 1992, we know of no operational program of microwave sea ice remote sensing in which quantitative signature

models are used to link observations with geophysical properties (save ice type).

The purpose of this chapter is to clarify the state-of-the-art in microwave signature modeling for sea ice, and in the process elucidate signature-controlling properties of sea ice. Our approach is to compare signature computations from several models with observations in two relatively simple, particularly well-characterized cases. The data set in each case consists of nearly simultaneous, ground-based, active and passive signature observations and independent ice and snow characterization data. We use the data to constrain model inputs and/or compare with model inputs used to match the observations, and we provide information on model sensitivities to input parameter variations. Although we restrict ourselves to models previously documented in the literature, the results and comparisons we present here are new. Our collection of models is not exhaustive, but we believe we have examples of every major type of model presently used in connection with sea ice. Our focus on small, intensively characterized regions of ice makes possible relatively clean comparisons of models with data, and thus sharpens the inferences we can draw. However, this focus also complicates immediate application of our results in interpreting airborne and spaceborne sensor data. We think it worthwhile to accept this temporary complication for the sake of gaining physical insight.

The plan of this chapter is as follows. Section 8.2 presents an overview of the models we employ. The first part of the overview discusses generally some major physical issues that may be treated differently in different models and notes the resulting practical implications. The second part consists of summaries of the individual models, specifically noting the ways in which each treats the major issues (the discussions are primarily physical rather than mathematical, but provide ample references). Readers desiring only the most essential discussions may wish to read only Sections 8.2.1, 8.2.2.1, 8.2.2.5, and the first paragraph or so of each subsection in Section 8.2. Section 8.3 treats our first case study, that of a thin (8 cm) sheet of congelation ice, growing rapidly without snow cover and similar to ice in quiescent Arctic leads, that was studied as part of the Cold Regions Research and Engineering Laboratory Experiment (CRRELEX) in January 1988. Section 8.4 similarly addresses a second case study concerning cold, snow-covered old ice observed as part of the Coordinated Eastern Arctic Research Experiment (CEAREX) in October 1988. This second case study involves two different regions on a single old ice floe—first, a fresh, raised area having a very low density upper layer, and second, a refrozen melt pond with an upper layer density much closer to that of pure ice. Section 8.5 concludes the chapter with a discussion of our finings in the broader context of microwave signature modeling and remote sensing of sea ice. We summarize what we have learned about the state of signature modeling from this study and offer a few caveats about what our results do not imply. Finally, we consider directions for future work on signature physics and remote sensing algorithms.

8.2 Overview of Signature Models

Signature modeling for geophysical media is based on idealization and approximation. The geometric arrangement of constituent materials, that is, the morphology of geophysical media, is often complicated. Therefore, an initial step in modeling is to abstract from the actual morphology an idealized geometrical representation in the hope that scattering from the idealized medium mimics that from the actual medium while being more tractable to compute. The choice of idealizations for any particular combination of geophysical medium, electromagnetic wavelength, polarization, etc. is typically not straightforward, but rather a matter of judgment. Choices differ between modelers, even with respect to exactly the same geophysical medium. Moreover, solving the equations of scattering almost always necessitates a number of approximations. Appropriate approximations depend on wavelength, electromagnetic lossiness of the medium, and so on, and are often also matters of judgment. The choices of idealizations and approximations essentially define a scattering model.

Section 8.2.1 is meant as an observer's guide to spotting the key differences between models and interpreting the following model-data comparisons. We assume on the part of the reader a qualitative understanding of scattering, including rough surface versus volume scattering, single versus multiple scattering, and the propagation and scattering of coherent versus incoherent waves within sea ice. A sufficient background for our purposes is available in Chapter 3 of this book. Section 8.2.2.1 supplements this material. We also recommend as background the reviews of basic passive, active, and polarimetric signature characteristics given in Chapters 4, 5, and 25, respectively.

8.2.1 Fundamental Physical Mechanisms and Effects

The first issue is whether a model derives signatures based on scattering from dielectric inhomogeneities within the medium alone (volume scattering), scattering only from roughness at interfaces in the medium (rough surface scattering), or from some combination of the two. Research over the past decade has produced an array of volume scattering models that may plausibly apply to at least some types of sea ice, and a corresponding array of physical idealizations and approximation schemes. Rough surface scattering models are presently fewer in number; there are correspondingly fewer choices to discuss. We therefore begin with a discussion of the main points on which volume scattering models may differ.

A fundamental distinction between volume scattering models concerns layering. Ice properties typically show pronounced variations with depth. Snow may cover the ice. Thus, signature models typically treat the air–snow–sea ice–seawater system as a stack of horizontal layers with planar or rough interfaces (Figure 8-1). (Lateral variations in ice properties and morphology are important. However, because models incorporating such variations are much

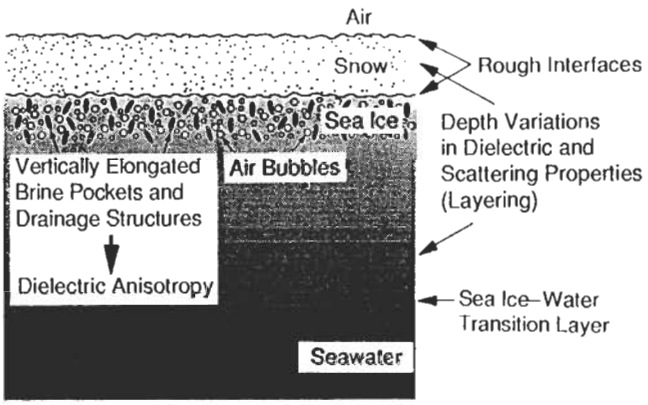

Fig. 8-1. The layered physical model of sea ice conceptually common to most sea ice signature models, including vertical variations in snow and sea ice properties and rough air–snow and snow–ice interfaces. The figure is schematic and not drawn to scale. Note that first-year ice contains many brine pockets at all depths, but few relatively small air bubbles. In old ice, the upper layers contain many relatively large air bubbles. Brine pockets are generally found in lower layers.

more difficult, and because we can partly account for lateral variation by using different models at different locations, current models do not generally address this issue. Neither has signature modeling for features such as ice ridges and thermal cracks received much attention; we therefore omit this topic from our discussion here. These matters may well require reconsideration, as we discuss in Section 8.5.) Models differ significantly in the number of scattering layers they treat. Perhaps even more significant is whether interactions of waves scattered or reflected from different layers are treated coherently or incoherently. When layer interfaces are nearly planar (measured in radiation wavelengths) and scattering in the layers is not too strong, waves reflected from layer interfaces remain coherent and thus interfere. Microwave signatures are strongly affected by this interference, and thus highly sensitive to layer thicknesses, radiation wavelength, and incidence angle (see, for example, Blinn et al. [1972]). Roughness of the layer interfaces, strong scattering within layers, or nonuniformity of layer thickness within the sensor footprint can destroy the coherence of contributions from different layers. Sensitivity to layer thickness is greatly decreased in this case. Most models treat field contributions as either completely coherent (e.g., strong fluctuation theory models) or completely incoherent (e.g., classical radiative transfer models). The appropriate choice of coherent or incoherent model in a given situation depends on the radiation wavelength, sensor bandwidth, uniformity of layer thickness and interface roughness, and so on, and may not be clear when first approaching a problem theoretically.

Another distinction between volume scattering models arises in the way they picture the spatial permittivity fluctuations inside the scattering medium. Discrete scatterer models envision a homogeneous dielectric background medium, in which are embedded discrete inclusions or particles of materials having permittivities different from that of the background. The random nature of the scattering medium in this picture is due to randomness in particle positions, sizes, and perhaps composition. Computational tractability often constrains particle shapes to be relatively simple (spheres or ellipsoids) and, in some instances, also constrains particle size or the size distribution. In contrast are so-called continuous random medium models in which permittivity fluctuations may be modeled as an arbitrary random function of position, characterized by its mean, variance, and spatial correlation. The term "continuous random medium model" is actually a slight misnomer because there is no restriction that the function describing the random permittivity fluctuations be continuous; indeed, two-point permittivity fluctuation statistics in discrete random media have been computed and used [Stogryn, 1984a, 1985, 1986; Vallese and Kong, 1981; Jin and Kong, 1985; Reber et al., 1987]. In fact, both of the models based on the continuous random medium model that we employ in this chapter (Sections 8.2.2.6 and 8.2.2.7) actually assume discrete inclusions of scattering material in the ice. The point, however, is that continuous random medium models are not restricted to discrete scatterers and may treat geometrically complex media directly.

It might seem preferable to avoid the restrictions of discrete scatterer models entirely and employ only continuous random medium models. In practice, however, the choice between these types of models is linked to a third important distinction between models, namely the degree to which they treat multiple scattering of the incoherent field. Recall from Chapter 3 that volume scattering may be thought of in terms of a coherent field which propagates down into the medium, decaying due to both absorption and scattering into incoherent fields (Section 8.2.2.1). When absorption is small and scattering is strong, the incoherent fields may themselves be scattered repeatedly. Discrete scatterer models, especially those that can be cast in the form of classical radiative transfer theory, are generally able to treat multiple scattering of the incoherent field. However, practical solutions of the field equations in continuous medium models have, to date, been restricted to cases where the incoherent field is only singly scattered (specific examples and references are given in Sections 8.2.2.6 and 8.2.2.7—note that this is a restriction in practice, not in principle). This limitation is evidently significant in some strong scattering cases such as the one we consider in Section 8.4. Thus, the distinction between models that treat multiple scattering of the incoherent field and those that do not is linked in practice to the choice of description for the random scattering medium. There is, at least at present, a tradeoff between generality in describing the scattering medium on one hand and the strength of scattering that can be treated on the other.

Turning to rough surface scattering models, one major idealization stands out. The probability distribution of surface heights at any n points on the surface is assumed to be homogeneous and jointly Gaussian in virtually all mod-

els currently applied to sea ice. The roughness of some ice types (e.g., pancake ice) may fail to satisfy these assumptions; thus interpretation of model-data comparisons may be aided by awareness of this idealization. Most models also assume that surface roughness statistics (e.g., correlation length) are independent of orientation on the surface, i.e., that surface roughness statistics are directionally isotropic. Variation between models can occur because of differing assumptions about the form of the surface roughness correlation function, or equivalently the spectrum of surface height variations. The most common choice is an exponential form for the correlation function. This choice is not strictly compatible with models that are derived assuming that the surface height possesses at each point a well-defined tangent plane, but ignoring this conflict often leads to reasonable results. The main division between models is the choice of approximation scheme. Models relying on conventional perturbation theory are, roughly speaking, restricted to surfaces whose height variations are much smaller than the radiation wavelength. Models that use the tangent plane approximation (collectively called physical optics models) are restricted to surfaces whose roughness is smoothly undulating on horizontal length scales comparable to the wavelength. New rough surface scattering models generally attempt to supersede the restrictions of these classical models.

A few issues are common to volume and surface scattering models. The first of these arises because the brine pocket and drainage structures of congelation sea ice (Chapter 2) cause a directional anisotropy in dielectric properties for this ice [Sackinger and Byrd, 1972; Bogorodskii and Khokhlov, 1977; Golden and Ackley, 1981]. The permittivity and absorption measured with electric fields oriented vertically (along the preferred direction of the structure) are notably larger than those measured in orthogonal directions (Chapter 3). This may be important in understanding the signatures of some ice types. However, models differ in whether and how they take account of this phenomenon. Models for passive microwave signatures may or may not take into account the ice temperature profile within the effective range of emitting ice depths. Finally, models may be polarimetric, nonrigorously polarimetric, or simply nonpolarimetric. Volume scattering models derived systematically from Maxwell's equations are in principle polarimetric, whether or not the effort has been expended to make any particular implementation of the model polarimetric. The same holds true of classical radiative transfer models. However, models derived from radiative transfer after many simplifications typically are not polarimetric. Surface scattering models based on conventional perturbation theory are also polarimetric. However, physical optics-based surface scattering models are, at best, nonrigorously polarimetric, because of the nonrigorous tangent plane approximation they employ.

8.2.2 Volume Scattering Models

8.2.2.1. General comments on models in the form of classical radiative transfer. The classical theory of radiative transfer for scattering in volume was developed extensively to treat propagation, emission, and scattering problems in stellar and planetary atmospheres, as well as various other media [Ishimaru, 1978, and references therein]. It has since found application in signature modeling for vegetation and for sea ice [Fung and Eom, 1982; Tsang et al., 1985; Ulaby et al., 1982]. Though at least some snow and sea ice signatures computed using classical radiative transfer depart seriously from reality (see below), its intuitive form and the store of solution techniques from classical theory provide strong motivations to cast modern theories, including several that we apply in this chapter, in the classical form. We therefore begin this section with a discussion of features common to these models by reason of their form, as well as some of the fundamental physical insight about scattering that classical radiative transfer provides.

The fundamental quantity in radiative transfer is the specific intensity I defined at any point in space $\mathbf{r}$ as the power flowing in a given direction $\hat{\mathbf{s}}$ per unit solid angle per unit emitting area per unit bandwidth, assuming unpolarized radiation. (To construct a fully polarimetric theory, the scalar specific intensity I is generalized to a vector quantity $\mathbf{I}$ whose components are the Stokes parameters of the wave at $\mathbf{r}$ propagating in direction $\hat{\mathbf{s}}$ per unit solid angle per unit emitting area per unit bandwidth.) The point $\mathbf{r}$ need not lie in the volume containing the scatterers. In the classical theory, an integro-differential equation which governs I as a function of position and direction is derived heuristically [Ishimaru, 1978, Chapter 7]

$$\frac{dI(\mathbf{r},\hat{\mathbf{s}})}{d\hat{\mathbf{s}}} = -\kappa_e I(\mathbf{r},\hat{\mathbf{s}}) + \int_{4\pi} d\hat{\mathbf{s}}' P(\hat{\mathbf{s}},\hat{\mathbf{s}}') I(\mathbf{r},\hat{\mathbf{s}}') + J(\mathbf{r},\hat{\mathbf{s}}) \quad (1)$$

where k_e is the extinction coefficient for coherent intensity, P is the so-called phase function relating scattering from direction $\hat{\mathbf{s}}'$ into direction $\hat{\mathbf{s}}$, and J is a thermal source term owing to emission within the scattering volume. In a polarimetric theory, the phase function and extinction coefficient generalize to 4¥4 matrices, and the emission source term generalizes to a vector with four components (see, for example, Tsang et al. [1985]). This equation, known as the equation of radiative transfer or transport equation, describes the total change in specific intensity in the direction $\hat{\mathbf{s}}$ as a sum of effects, namely extinction, scattering from other directions into the direction $\hat{\mathbf{s}}$, and thermal emission into that direction. Note that the extinction coefficient k_e results not only from absorption but also from scattering out of direction $\hat{\mathbf{s}}$ into other directions. Because Equation (1) is a first order differential equation, it is necessary to specify boundary conditions, one for each region in which

the equation is to be solved, to completely specify the problem.

An equation relating the phase function P, the single-scattering albedo, $\tilde{\omega}$, and κ_e results from the statement of energy conservation:

$$\int_{4\pi} d\hat{\mathbf{s}}\, P(\hat{\mathbf{s}}, \hat{\mathbf{s}}') = \kappa_e \tilde{\omega} \leq \kappa_e \tag{2}$$

where the equality holds in the lossless case, i.e., when no absorption takes place in the background medium or in the scatterer. Physically, this equation states that the power scattered out of direction $\hat{\mathbf{s}}'$ must not exceed the total power loss for intensity traveling in the direction $\hat{\mathbf{s}}'$; in the case of no absorption, these powers must balance.

An approximate solution method for the transport equation can be used to gain some additional physical insight into the scattering process. Suppose for a moment that the albedo, $\tilde{\omega}$, is small compared to one. Then it is reasonable to attempt a zeroth-order solution to the transport equation inside the scattering volume by simply ignoring the integral term on the right-hand side of Equation (1) (which is effectively proportional to $\tilde{\omega}$). Neglecting also thermal emission for the moment, the specific intensity to zeroth-order in albedo satisfies the equation

$$\frac{dI_0(\mathbf{r}, \hat{\mathbf{s}})}{d\hat{\mathbf{s}}} = -\kappa_e I_0(\mathbf{r}, \hat{\mathbf{s}}) \tag{3}$$

The extinction coefficient k_e is real and positive; thus the zeroth-order specific intensity is simply a real exponential function that decays on the length scale $1/k_e$ in the direction of propagation through the medium. (The boundary conditions merely determine position-dependent factors and additive constants.) $I_0(\mathbf{r}, \hat{\mathbf{s}})$ contains the effects of absorption and scattering out of the direction $\hat{\mathbf{s}}$, but no effect of scattering from other directions into $\hat{\mathbf{s}}$. The latter effect first enters in the first-order solution, the equation for which is obtained by substituting $I_1(\mathbf{r}, \hat{\mathbf{s}})$ for the unknown I in Equation (1).

$$\frac{dI_1(\mathbf{r}, \hat{\mathbf{s}})}{d\hat{\mathbf{s}}} = -\kappa_e I_1(\mathbf{r}, \hat{\mathbf{s}}) + \int_{4\pi} d\hat{\mathbf{s}}' P(\hat{\mathbf{s}}, \hat{\mathbf{s}}') I_0(\mathbf{r}, \hat{\mathbf{s}}') \tag{4}$$

Thus, the specific intensity to first-order in albedo contains the effects of single scattering of the zeroth-order intensity which itself contains the effects only of absorption and scattering out of beam. This idea is similar in spirit (if not precisely in detail) to that in the distorted Born approximation discussed below (cf. Section 8.2.2.5): incoherent intensity is generated by single scattering of fields which themselves contain effects of only absorption and (multiple) coherent forward scattering. The idea extends naturally: in more strongly scattering cases, second-order intensities result from scattering of the singly scattered first-order intensities, third-order intensities result from scattering of second-order intensities, and so on. This iterative approach is sometimes actually used for the numerical solution of radiative transfer and other multiple scattering theories. However, when the albedo is not small and scattering volumes are large (allowing more opportunities for multiple scattering), direct numerical solutions of equations such as Equation (1) are often more practical.

The chief assumptions in the derivation of Equation (1) are a lack of correlation between fields traveling in distinct directions and the independence of fields scattered from different locations or particles [Ishimaru, 1978; Tsang et al., 1985; Ulaby et al., 1982]. Thus coherent interaction, i.e., interference, between waves from different layers is not accounted for in classical radiative transfer. As noted at the beginning of this section, this neglect may in some cases be a source of error, while in others, especially those involving irregular layers, it may actually be an asset.

Solution of the transport equation requires the specification of boundary conditions at the layer interfaces. Boundary conditions for flat and rough interfaces have been developed and used in practice [Tsang et al., 1985; Ulaby et al., 1982]. Thus classical radiative transfer theory offers a way to treat the combined effects of volume and rough surface scattering. This is true as well for at least two of the models described below (dense medium radiative transfer and dense medium theory) that take the form of classical radiative transfer. However, this combined treatment is limited to incoherent interaction between waves scattered from the interfaces and in the volumes.

A classical radiative transfer model with rough interfaces has been used with some success to fit sea ice signatures [Fung and Eom, 1982]. However, a number of authors observed that radiative transfer models predicted erroneous signatures, especially for snow, when driven by input parameters derived from independent characterization measurements [Stogryn, 1986, and references therein]. Judging from passive signature observations, it appears that the classical assumption of independent scattering from distinct spatial regions or particles causes an overprediction for scattered intensities, thus lowering predicted brightness temperatures to unrealistic levels (however, see also Section 8.2.2.4). In retrospect, this may be understandable; the classical theory was developed to treat cases where scatterers occupied less than 1% of the total scattering volume. The scattering particles in snow and sea ice typically occupy 5% to 50% of the scattering volume; effects of one scatterer on the contribution of another, in addition to classical multiple scattering, can therefore become appreciable. Such effects are generically termed dense medium effects. While dense medium effects led Stogryn, Kong, and others to investigate strong fluctuation theory, others sought to develop alternative models in the form of classical radiative transfer that would account for nonindependent scattering. We employ three of the resulting models in our case studies and summarize the physical

content of these models in subsections 8.2.2.3, 8.2.2.4, and 8.2.2.8. We first summarize a simpler model with its conceptual roots in the first-order physical picture of Equation (4).

8.2.2.2. Independent Rayleigh-scatterer layers. Most of the models used in this chapter are based on recent developments in the theory of wave scattering in random media; they are therefore sophisticated and, to nonspecialists, probably arcane. We do not yet understand which situations require the sophistication of the new models. It is therefore desirable to include in our study a physical model based on relatively simple, intuitive considerations, but which nonetheless has a reasonable basis in scattering physics. Drinkwater [1989, 1987], Drinkwater and Crocker [1988] and Livingstone and Drinkwater [1991] have recently applied such a model for backscattering from sea ice (the model is for backscattering only; passive signatures are not treated). The essence of the model was proposed by Attema and Ulaby [1978] for vegetation, and a version more appropriate for sea ice was later given by Kim et al. [1984a, b, 1985] (see also Section 11-5 of Ulaby et al. [1982]). In this chapter we employ a slight extension of the model to allow for two volume scattering layers within the ice. This feature permits us to address backscattering from low-density old ice with two layers in our second case study. The single layer version is similar to that used by Ulander et al. [1992] in connection with observations from the Bothnian Experiment in Preparation for ERS-1 (BEPERS).

This model pictures the snow-ice system as a snow layer overlying two ice layers (Figure 8-1). Each layer contains discrete volume scatterers; these are ice grains in snow, air bubbles in ice. (Generally, the snow layer may be wet and volume scattering from water inclusions is also modeled; however, this situation does not arise in our study.) The layers are assumed horizontally uniform with constant thickness; the scatterers are assumed uniformly distributed within each layer. The volume scatterers in each layer are assumed much smaller than the radiation wavelength and modeled as Rayleigh-scattering spheres. The layer densities and sphere radii (or more generally the distribution of sphere radii) are to be specified from ice and snow characterization data. The model does not presently treat any effect of dielectric anisotropy in congelation ice.

The scattering model is based on the idea illustrated in Equation (4), together with a partial accounting for rough surface scattering effects. The total backscattering cross section is modeled as an incoherent sum of component cross sections, each identified with a particular rough interface or volume scattering layer [Drinkwater and Crocker, 1988; Kim et al., 1985]:

$$\sigma^0_{\text{total}} = \sigma^0_{as}(\theta) + T^2_{sa}(\theta') \times \left\{ \exp\left(-2\kappa_e\, d / \cos\theta'\right) \left[\sigma^0_{si}(\theta') + \sigma^0_i(\theta') \right] + \sigma^0_s \right\} \quad (5)$$

where q is the angle of incidence, θ' is the angle of refraction in the snow layer corresponding to incidence angle θ (assumed real because the imaginary part of the snow permittivity is assumed much smaller than the real part), $T_{sa}{}^2(\theta')$ is the Fresnel power transmission coefficient between air and snow (horizontally polarized for HH backscattering, vertically polarized for VV), d is the snow layer thickness, κ_e is the snow extinction coefficient, and σ^0_{as}, σ^0_s, σ^0_{si}, and σ^0_i are the backscattering cross section contributions of the air–snow interface, the snow layer, the snow–ice interface, and the ice volume, respectively. The permittivity of the snow layer (which is dry in our case studies) is computed from an empirical formula and used to calculate κ_e for the snow and T_{sa}. The snow volume scattering term is given by

$$\sigma^0_s(\theta') = T^2_{sa}(\theta')\left[1 - \exp\left(-2\kappa_e\, d / \cos\theta'\right)\right] \quad (6)$$

where σ_v is the volume scattering cross section per unit volume of the snow crystals embedded in air. Equation (6) results by integrating the backscattered power contributions from each depth in the scattering layer, accounting at each depth for extinction of the illumination and backscattered contribution in the part of the layer above that depth [Ulaby et al., 1982, Section 11-5.3]; thus, the correspondence between this model and Equation (4). A further correspondence is the assumption that scattered intensity contributions from neighboring ice grains add incoherently. Thus $\sigma_v = \int dr\, N(r)\, \sigma_g(r)$ where σ_g is the Rayleigh backscattering cross section for a single spherical ice grain and $N(r)$ is the number of grains per unit volume of snow with radii between r and $r + dr$. The total volume of ice per unit volume of snow is $4\pi/3 \int dr\, r^3 N(r)$; this latter number can be determined independently by a measurement of bulk snow density.

The form of the equation for the ice volume scattering term, σ^0_i, in Equation (5) is similar to Equation (6) but contains two terms, one for each bubbly layer; the transmission coefficients in these terms refer to transmission at the snow–ice and ice layer interfaces, the extinction coefficients refer to extinction with the ice layers, refracted angles are computed within each layer, and so on. The permittivity of bubbly ice is estimated using a Polder–van Santen type formula given by Fung and Eom [1982]. The Rayleigh-scattering bubbles are then assumed to reside in an effective background having the effective permittivity (which is smaller than that of pure ice by an amount depending on density). This lowers the cross sections of individual bubbles in low density layers compared with identically sized but less numerous bubbles in higher density layers (Section 8.4.2.1). In the model results given below, extinction is computed on the basis of absorption alone. Scattering out of beam is neglected, but this should minimally affect computed backscattering levels for the scattering extinction coefficients and layer thicknesses in our cases.

Any reflection or scattering at the interface between ice layers is neglected. The rough surface scattering cross sections, σ^0_{as} and σ^0_{si}, are computed according to a physical optics model using interface roughness statistics from characterization data (Section 8.2.3.1). Note that the model treats no multiple scattering, scattering before or after reflections from layer interfaces, or coherent interaction between contributions from different layers. The model is not polarimetric, and in fact contains little polarization dependence. The backscattering cross sections for the air–snow and snow–ice interfaces contain some polarization dependence (Section 8.2.3.1), but volume scattering is polarization dependent only because transmission across layer interfaces differs for vertical and horizontal polarization. The backscattering within the volume is polarization independent. Note also that the treatment of surface scattering in Equation (5) accounts neither for the change in effective illumination of snow volume scatterers due to the sprays of energy from snow–ice and air–snow interfaces nor for any other interactions between surface and volume scattering.

To summarize, this model is based (like classical radiative transfer theory) on independent scattering. Moreover, it neglects a number of effects included in many radiative transfer models. Given the previous difficulties found in comparisons between observations and signatures computed using classical radiative transfer (Stogryn [1986] and Section 8.2.2.1), there is reason to question the applicability of this model to snow and sea ice. On the other hand, it does include significant nonclassical, if ad hoc, modifications to account for dense medium effects, particularly the reduction of scattering from bubbles in low-density ice layers. Thus it is uncertain, prior to a comparison such as ours, whether the model just described can accurately predict active signatures of sea ice. In view of this uncertainty, the relative simplicity of this model, and the ease with which we can isolate different physical effects in it, argue strongly for its inclusion in this study.

8.2.2.3. Dense medium radiative transfer. Dense medium radiative transfer (DMRT) [Tsang and Ishimaru, 1987; Tsang, 1987] is a discrete scatterer model, i.e., it proceeds from a physical model for the scattering medium (snow or sea ice) consisting of discrete, regularly shaped particles embedded in a homogeneous background medium. Particle positions are correlated for media in which the volume of particles exceeds a few percent of the total volume of scattering material. The essential physical effect in DMRT is interference between scattered field contributions from neighboring particles, even in the ensemble average over all particle arrangements. The interference is governed by the correlations between particle positions; for particles small compared with the radiation wavelength (i.e., for Rayleigh scattering particles), this interference is effectively destructive and results in less scattering than would be predicted based on an independent scattering assumption. Thus, for a given set of input parameters, higher brightness temperatures and lower scattering cross sections are computed using DMRT than are computed using classical radiative transfer theory.

The derivation of DMRT proceeds from exact multiple scattering equations based on Maxwell's equations, using a series of consistent approximations for the coherent and incoherent scattered fields. Specifically, Dyson's general equation for the coherent field is first approximated using the quasicrystalline approximation with coherent-potential (QCA-CP). This approximation is sufficiently powerful to treat densely packed volumes of scatterers with permittivities differing strongly from their background; in this case, the real part of the effective propagation constant for the mean field may differ appreciably from the propagation constant in the background medium. Second, the ladder approximation for the intensity operator is applied in the general Bethe–Salpeter equation for the incoherent field. The ladder approximation accounts for that cascade of uncorrelated scattering events in the incoherent field that can each be described in terms of the two-point statistics of particle positions; DMRT thus presumes that such events dominate multiple scattering of the incoherent intensity. Within a densely packed medium, interscatterer separations range from near- to far-field values (i.e., some scatterers are within the near-field region of others). The wave interactions at all ranges are included in DMRT by using exact wave transformations from one scatterer center to the next. The result is a theory in the form of classical radiative transfer (the polarimetric version of Equation (1) where the extinction rate κ_e and albedo $\tilde{\omega}$ are given by expressions that agree with the classical expressions in the limit of small particle volume fractions but generally depend on correlations between particle positions). The phase matrix, extinction coefficient, and albedo satisfy energy conservation.

Tsang and Ishimaru [1987] and Tsang [1987] first developed DMRT for the case of a scattering layer containing Rayleigh-scattering spheres with a single radius. They assumed that the function describing the correlation between scatterer positions, that is, the pair-correlation function, could be approximated by the Percus–Yevick pair-correlation function derived in statistical mechanics. Under these assumptions, the complex effective wavenumber of the coherent field, including effects of both scattering and absorption, may be found by the procedure of Wen et al. [1990] (see, in particular, Section II). Tsang [1991] generalized the theory to treat Rayleigh-scattering spheres with a distribution of sizes. The DMRT phase matrix for these cases is identical to that in the classical theory, but albedos depend on correlations between scatterer positions. Expressions for the albedos are given with effective permittivity algorithms in each of the above references.

Because DMRT takes the form of radiative transfer, the array of solution methods developed for the classical theory may also be applied to this model. The present implementation of the theory employs the discrete eigenvalue-eigenvector method and treats two scattering layers over a nonscattering basement. The theory and implementation

are fully polarimetric. Interference between waves reflected from the various layer interfaces is neglected just as in classical radiative transfer theory. Particle shapes in the present theory and implementation are restricted to spheres, and sizes are presently limited to the regime in which Rayleigh scattering is valid. The spherical particle restriction precludes modeling of any effects of dielectric anisotropy in the ice; thus DMRT is likely to be most appropriate in old ice or other ice that is, to a good approximation, dielectrically isotropic. The theory requires input information on the permittivities of the background material (ice in sea ice, air in snow), scatterers (air bubbles in old ice, ice grains in snow), and especially on the size and size distribution of scatterers in the various layers. Winebrenner et al. [1989] provide information on signature sensitivities due to variations in bubble size, ice salinity, and density in a DMRT model with a single bubble layer containing bubbles of a single size.

8.2.2.4. Dense medium theory. Dense medium theory [Fung and Eom, 1985] is also a discrete scatterer model for spheres much smaller than the radiation wavelength, the form of which is the same as that of classical radiative transfer, Equation (1). The essential physical difference between dense medium theory and the classical theory is a modification of the phase matrix, and therefore also the extinction coefficient. Classical radiative transfer uses the Rayleigh scattering phase matrix for small spheres. Fung and Eom [1985] rederived the phase matrix using Mie coefficients for terms in the spheres' fields that fall off in range faster than $1/r$. The total scattering cross section (per unit volume of the scattering material) is computed by integrating the modified phase function over all solid angles, then added to the absorption cross section from Mie theory to obtain the extinction coefficient. Thus this theory considers a key physical effect of densely packed scatterers to be a near-field interaction between neighboring scatterers. This theory does not rule out neighboring-scatterer interference but does not account for it. The theory does not at present specify conditions under which either its near-field terms or interference may predominate, or predict when both effects must be considered.

Based on its modifications to classical theory, dense medium theory predicts an increase in scattering over that computed from the classical theory. Fung and Eom [1985] show backscattering cross sections computed for snow at 7–10 GHz assuming a single particle size. The cross sections are 1–3 dB higher than those predicted by classical radiative transfer; computed snow brightness temperatures in the same frequency range are 1–8 K lower than classical values. Fung and Eom [1985] report a better match to snow backscattering data using dense medium theory than that achieved using classical theory, and extinction calculations based on this theory are consistent with optical data reported by Vedernikova and Kabanov [1974]. However, the dense medium passive signature predictions are opposite to what would narrow the discrepancy in snow noted by Stogryn [1986] and others. The nonclassical effects predicted by dense medium theory decrease with increasing frequency and increasing particle radius, but increase monotonically for scatterer volume fractions between 0% and 30%, at least in the example given by Fung and Eom [1985].

In its present implementation, the theory treats a single scattering layer overlying a nonscattering basement. The layer need not be isothermal; this theory computes brightness temperatures directly, rather than emissivities, accounting fully for the temperature profile in the ice layer. The theory currently does not treat size distributions of scatterers, but rather fixes all scatterer radii at a single effective value to be determined on the basis of independent characterization information. The restriction to spherical scatterers also precludes modeling of the dielectric anisotropy in congelation ice. The classical form of the dense medium theory permits the use of the classical layer doubling method for solution [Ulaby et al., 1982]. The interaction of waves reflected from the layer interfaces is therefore incoherent, just as in the classical theory; results are therefore relatively insensitive to layer thickness. A rough surface boundary condition is employed at both the upper and lower layer interfaces. The results in this chapter were computed using the Integral Equation Method of Fung et al. [1991] for the elements of the boundary condition matrix (see Section 8.2.3.3).

8.2.2.5. General comments on strong fluctuation theory. The term strong fluctuation theory (SFT) refers to a class of volume scattering models that (1) employ the continuous random medium model to describe the scattering medium and (2) address the problem of strong contrasts in the permittivity of constituents of the scattering medium. For sea ice, the strong contrasts are those between the background pure ice and inclusions of brine and air. The correct treatment of such contrasts requires decomposition of integrals involving the dyadic Green's function for the electric field into sums of two terms. One term is a principal value integral with a volume around the source point excluded. The shape of this exclusion volume is determined by the shape and orientation of the scatterers and/or equicorrelation surfaces of the random permittivity [Stogryn, 1983a, b, 1984b; Tsang et al., 1985]. The second term consists of an integral over a product of terms, including a delta function centered on the source point times a dyad whose elements depend on the shape of the exclusion volume.

The fundamental random quantity in SFT is a second-rank tensor (which may be written in the form of a matrix), usually denoted $\bar{\bar{\xi}}$. Its elements depend on (1) the fluctuations of permittivity in the scattering medium and (2) the elements of the dyad associated with the delta function above, and thus the shape of the exclusion volume. The spatial cross-correlations between elements of $\bar{\bar{\xi}}$, as functions of lag, govern scattering of both the coherent and incoherent fields in SFT. For a scattering medium with only two components (e.g., pure ice and brine), a direct connec-

tion can be made between normalized (scalar) correlation functions of elements of $\bar{\bar{\xi}}$ and geometrical correlations of positions of inclusion material (e.g., brine) [Stogryn 1984a; Lin et al., 1988; Yueh et al., 1990]. Scattering media containing inclusions of more than one material (e.g., brine and air in ice, or ice and water in an air background) require the use of multiple geometrical correlations [Stogryn 1984a, 1985, 1987].

The coherent field in SFT is computed according to the bilocal approximation in Dyson's general equation for the coherent field [Stogryn, 1983a, 1984b; Tsang et al., 1985]. The bilocal approximation in Dyson's equation accounts for a cascade of uncorrelated single-scattering events, assuming that the coherent wave travels between events with a propagation constant equal to that in the background ice. The resulting effective permittivity includes an imaginary part due both to absorption and to extinction of the coherent field by scattering into the incoherent field. The bilocal approximation is believed to be accurate when the energy carried by the coherent field dominates the total energy flowing in the ice (due to both coherent and incoherent fields). The equation for the effective permittivity in the bilocal approximation can be solved analytically in the low frequency limit, i.e., when the correlation lengths of permittivity fluctuations are much smaller than the radiation wavelength [Tsang et al., 1985, Section 5.4; Stogryn, 1984b], and numerically at higher frequencies [Stogryn, 1986]. Both of the SFT models used in this chapter employ the low frequency, analytical solution for the bilocal approximation.

Both of the SFT models used in this chapter also compute the incoherent scattered field using the distorted Born approximation. This approximation accounts for contributions to the incoherent field that arise from scattering directly out of the coherent field, but not for any repeated, i.e., multiple, scattering of the incoherent field (cf. Section 8.2.2.1). Thus this approximation inherently limits the strength of scattering that can be treated. However, this limit is merely consistent with limitations inherent in the bilocal approximation for the coherent field [Stogryn, 1985]. Because of this sequence of approximations, the strong fluctuation theory models used in this chapter are sometimes termed multiple-forward-scatter, single-backscatter models.

The strong fluctuation theory models discussed below are purely volume scattering models, and interfaces between volume scattering layers are assumed planar. These models treat the interaction between waves reflected from layer interfaces coherently, and thus display layer thickness-dependent interference effects.

8.2.2.6. Polarimetric strong fluctuation theory. A fully polarimetric SFT model has recently been developed for a system of two scattering layers over a nonscattering halfspace [Nghiem, 1991, and references therein]. We term this model polarimetric SFT because it is fully polarimetric in its present implementation, and to distinguish it conveniently from the other, quite distinct, SFT model that we also apply in this chapter. In polarimetric SFT, the strong permittivity fluctuations due to individual brine pockets or air bubbles are directly responsible for volume scattering within the sea ice. (Contrast this mechanism with that in the SFT model of Section 8.2.2.7.)

The individual scatterers are, in general, modeled as ellipsoidal particles of identical size. The spatial distribution of scatterer locations within the layers is uniform. In sea ice, the ellipsoids represent brine pockets and have their longest dimension aligned with the vertical to represent the preferred vertical direction observed in brine drainage structure. Individual brine pockets have an ellipsoidal cross section in the horizontal plane to represent the observed horizontal anisotropy of brine pockets sandwiched between ice platelets within a congelation sea ice crystal (Chapter 2). The azimuthal orientation of platelet structure, i.e., the horizontal direction of c-axis alignment, typically varies randomly between crystals (except in exceptional cases such as fast ice, where ocean currents may align the platelet structures). Thus, moving from scatterer to scatterer in a given realization of the scattering medium, the azimuthal orientation of the shortest axis of the ellipsoid varies randomly with a uniform distribution between 0 and 2π radians. When the lengths of the horizontal ellipsoid axes differ significantly, the local permittivity fluctuations have a pronounced azimuthal anisotropy, whereas the large-scale properties of the scattering layer are always azimuthally isotropic. In snow, the axes of the ellipsoids are chosen to have the same length to reflect the isotropy of typical snow [Vallese and Kong, 1981].

The general ellipsoidal scatterer shape, the consequent local anisotropy, and the fully polarimetric computations are key features of this most recent SFT model [Nghiem, 1991]. An important consequence of local azimuthal anisotropy in the sea ice layer is the prediction of substantial cross-polarized backscattering. Such a prediction differentiates this model from other models that use the first-order distorted Born approximation with a representation for the scattering medium that is azimuthally isotropic on the large scale. This model therefore predicts new and first-year ice signatures with much higher cross-polarized backscattering cross sections than those predicted by other SFT models.

Because the scatterers are nonspherical and randomly oriented, the exclusion volume (Section 8.2.2.5) in this model varies from scatterer to scatterer [Nghiem, 1991; Yueh et al., 1990]. Thus the normalized spatial correlation at lag $\mathbf{r}$ between any pair of elements of $\bar{\bar{\xi}}$ is expressed in terms of a correlation function, $R_\phi(\mathbf{r})$ which is conditioned on the azimuthal scatterer orientation angle ϕ. Expressed in local coordinates $\mathbf{r} = \hat{\mathbf{x}}\, x + \hat{\mathbf{y}}\, y + \hat{\mathbf{z}}\, z$ appropriate to a given scatterer,

$$R_\phi(\mathbf{r}) = \exp\left[-\left(\frac{x^2}{l_x^2} + \frac{y^2}{l_y^2} + \frac{z^2}{l_z^2}\right)^{1/2}\right] \tag{7}$$

Nghiem [1991] has coined the shorthand term "local correlation function" for this quantity. The correlation lengths l_x, l_y, and l_z are related to the axial dimensions of the scatterers (i.e., brine pockets or air bubbles in sea ice, and ice grains in snow). However, the correspondence is not precise for the following reasons. The actual scatterers in snow and sea ice have a distribution of sizes. The correlation lengths (and thus scatterers) are much smaller than the radiation wavelength, according to assumptions made in this model (Section 8.2.2.5). For scatterers much smaller than the radiation wavelength (i.e., Rayleigh scatterers), the strength of scattering increases rapidly and nonlinearly with increasing scatterer size. Thus larger, less numerous scatterers can contribute more to the total amount of scattering than the more abundant, smaller scatterers. Any single, effective correlation length used to characterize the scatterer size should therefore exceed the actual mean scatterer size by an amount depending on the shape of the size distribution [Jin and Kong, 1985]. At present, the effective correlation lengths in Equation (7) are chosen partly on the basis of model fitting and partly on the basis of independent thin section analysis such as that of Lin et al. [1988] and Perovich and Gow [1991]. (Thus this practice is a departure from that in work by Lin et al. [1988] using an earlier SFT model.) Typical correlation lengths in sea ice range from tenths of millimeters to millimeters, with the longer dimension in the vertical (l_z). The correlation functions for snow layers are spherically symmetric, i.e., $l_x = l_y = l_z$, and the correlation length is on the order of tenths of millimeters [Vallese and Kong, 1981; Reber et al., 1987].

As per the discussion above, the local azimuthal orientation of the correlation function in Equation (7) is assumed to be random with a uniform distribution over all possible horizontal directions. The effective permittivity, backscattering cross sections, and, for polarimetric signatures, elements of the Mueller and covariance matrices (Chapter 25) are computed by averages over the local azimuthal orientations. The resulting (tensor) effective permittivity is azimuthally isotropic but reflects a dielectric anisotropy between vertical and horizontal directions due to vertically elongated brine pockets [Nghiem, 1991]. The local azimuthal anisotropy locally couples electric fields of any given polarization into orthogonally polarized fields, and this is reflected in the backscattering signatures (for a somewhat simpler example of this phenomenon, see Yueh et al. [1990]).

Emissivity is computed in this model assuming that the ice is isothermal so Kirchhoff's law relates emissivities and reflectivities. However, because the model is polarimetric, polarimetric passive microwave signatures may also be computed.

8.2.2.7. Many layer strong fluctuation theory. Stogryn has developed a model also based on strong fluctuation theory, but which is substantially different from that described in Section 8.2.2.6 [Stogryn, 1983a, b, 1984a, b, 1985, 1987]. He has applied this theory to study the effective (tensor) permittivity of sea ice [Stogryn, 1987], but to our knowledge has not yet published signature computations for sea ice in the literature. We apply here an implementation of Stogryn's theory by Grenfell which computes both active and passive signatures. We have termed this implementation the "many layer strong fluctuation theory" because (1) it treats problems with many layers (as many as 30 in the present implementation), (2) it is not fully polarimetric (although there is no fundamental barrier to making it so, and (3) this model is distinguished from that described in the previous subsection. Like polarimetric SFT, the many layer theory is based on the bilocal and distorted Born approximations. It also treats interference between waves reflected and transmitted through the various layer planar interfaces coherently. This theory is based fundamentally on the continuous random medium model; however, it assumes a very different picture for the sea ice scattering medium and for the ultimate cause of scattering than in the polarimetric SFT model.

Stogryn [1987] first applies strong fluctuation theory within individual sea ice crystals assuming an aligned array of ice platelets with vertically elongated brine pockets sandwiched between them. He computes a directionally anisotropic, polarization-dependent (i.e., tensor) effective permittivity for a single ice crystal of size on the order of 1 cm. Any air bubbles in the ice are assumed to lie around the edges of crystals. The effective permittivity varies from crystal to crystal because the orientation of platelet structures varies between crystals. These orientations are assumed uncorrelated and uniformly distributed through all azimuthal angles from 0 to 2π. It is the fluctuation of permittivity within the jumble of crystals that causes scattering, according to this model. The contrast in permittivities between crystals is smaller than that between brine and ice (the driving fluctuation in the previous model), but crystals are larger than brine pockets. This approach does produce a cross-polarized backscattering response, but the response is weaker than that produced by the polarimetric SFT model.

The many layer model takes as input profiles of ice temperature and salinity with depth. It uses the equations of Frankenstein and Garner [1967] to compute brine volume, and then computes effective and fluctuating permittivities using assumptions about brine pocket and crystal geometry and spacing. Thus the need for direct measurements of permittivity correlation functions is avoided at the expense of having to assume values for parameters specifying brine pocket geometries. Permittivity of the brine pockets is set using the equations of Stogryn and Desargent [1985]. The most significant tunable parameters are the mean tilt angle of the long axes of brine pockets with respect to vertical and the ratio of brine pocket length to width. Stogryn [1987] has suggested for these parameters values of 24° and 200, respectively, based on model fits to extinction data. However, these values differ from estimates taken directly from saline ice samples [Arcone et al., 1986; Lin et al., 1988]. Parameters relating to the geometry of liquid water in wet snow are also significant

and poorly known, but do not affect the studies we present below.

Like polarimetric SFT, this model computes emissivities on the basis of Kirchhoff's law, which relates emissivity to reflectivity. Thus although the model accounts for effects of the true ice temperature profile on brine volume, and therefore on the effective permittivity, it does not fully account for any effects this profile may have on emission.

8.2.2.8. Modified radiative transfer. Modified radiative transfer (MRT) [Lee and Kong, 1988; Lee and Mudaliar, 1988; Mudaliar and Lee, 1990] is a model in the general form of classical radiative transfer based on the continuous random medium model. The model is derived on the basis of consistent multiple scattering approximations for both coherent and incoherent fields. The primary aim of MRT is to capture the general, partially coherent interaction between field contributions from different layers in the scattering medium (layer interfaces are assumed planar). To this end, the theory retains correlations between upgoing and downgoing waves at the same angles in each layer. The interactions appear in additional terms on the right-hand side of the MRT analog to Equation (1). This permits the study of coherent interaction effects as functions of volume scattering strength, layer optical depth, and other factors. Results from our first case study (Section 8.3) suggest the potential relevance of these effects.

The derivation of MRT begins with a continuous random medium in which permittivity fluctuations may be strong; the initial development is essentially the same as that in strong fluctuation theory. The dyadic Green's functions are decomposed into singular and nonsingular parts; the singular parts are treated carefully. However, MRT computes the coherent field using the nonlinear approximation in Dyson's equation. Recall from Section 8.2.2.5 that the bilocal approximation assumes that the coherent field travels between scattering events with the propagation constant appropriate for the background ice. By contrast, the nonlinear approximation assumes a propagation constant equal to the effective propagation constant of the sea ice, and thus accounts for additional multiple forward scattering events in the coherent field. The nonlinear approximation is roughly the continuous-medium analog to the QCA-CP approximation in DMRT (cf. Section 8.2.2.3). MRT then computes the incoherent scattered field, accounting for a (presumably predominant) class of multiple scattering events in the incoherent field as well. Specifically, MRT makes use of the general Bethe–Salpeter equation for the incoherent field and the ladder approximation for the intensity operator in this equation (also in a kind of continuous-medium analog to DMRT). The ladder approximation accounts for that cascade of uncorrelated scattering events in the incoherent field that can each be described in terms of two-point permittivity statistics. The combination of the nonlinear and ladder approximations produces a self-consistent theory in terms of energy conservation. Including some multiple scattering of the incoherent field would seem to permit MRT to treat stronger scattering than theories using the distorted Born approximation. However, solution of the nonlinear approximation equation for the coherent field remains restricted to the low-frequency regime. The net effect of this restriction is not presently clear.

MRT was first developed for electromagnetic wave scattering by Zuniga and Kong [1980] [Tsang et al., 1985, Section 5.5]. Lee and Kong [1985a, b, 1988] generalized the theory to treat dielectrically anisotropic scattering media such as saline ice. However, the solutions of the theoretical equations to date [Lee and Mudaliar, 1988; Mudaliar and Lee, 1990] are restricted to a single, infinitely thick scattering layer; the only layer interface is at the top of the layer. Thus there can be no interactions of waves from different layers. The present solutions are also limited to first-order scattering; this is analogous to Equation (4) and essentially equivalent to the distorted Born approximation. The present solution is also restricted to isothermal emitting media. Mudaliar and Lee [1990] have successfully matched some passive signature observations for old ice at microwave and millimeter-wave frequencies using this solution. However, because of the present restrictions we will not be able to demonstrate the full capability of MRT in this chapter. Rather, the initial results we present are intended as a spur to further research.

The continuous random medium model upon which MRT is built has yet to be specialized to model sea ice. Thus, the present version of MRT requires direct specifications for the mean, variance, and correlation length of permittivity fluctuations within the ice. In the case of dielectric anisotropy, two such sets of statistics are required, one for fluctuations in the preferred direction in the ice (which need not be vertical), one in an orthogonal direction. These statistics may in principle be supplied directly from independent ice characterization measurements such as those of Perovich and Gow [1991], but at present must often be set according to the modeler's judgment.

8.2.3 Rough Surface Scattering Models

Our concern with rough surface scattering in this chapter is confined almost entirely to its effect on backscattering signatures. Only one of the models we employ for passive signatures currently includes rough surface scattering effects (namely, the dense medium theory/integral equation method). We use this model to compute passive signatures in only one case, that of thin gray ice, and in this case the effects of surface roughness on emission are minor. Thus, the following summaries focus on backscattering characteristics of rough surface scattering models.

8.2.3.1. Physical optics under the scalar approximation. The common element in all models based on physical optics is the so-called tangent plane approximation. The fundamental unknowns in rough surface scattering problems are the source densities of Huygens' wavelets induced on the surface by the illumination. The tangent plane approxima-

tion replaces, at each point on the rough surface, the unknown source density by the density that would exist if, instead of the actual surface, there existed at that point a plane tangent to the actual surface, separating the same dielectrics actually separated by the rough surface. Thus physical optics models are valid only for surfaces that undulate smoothly on horizontal length scales comparable to the radiation wavelength; their validity at large incidence angles is also problematic [Thorsos, 1988]. A more quantitative statement of this restriction depends on the form of the surface roughness correlation function, but most authors [Ulaby et al., 1982; Thorsos, 1988] seem able to agree on a criterion $kL \gtrsim 2\pi$. When the standard deviation of surface heights is large compared with the wavelength, physical optics reduces to the familiar geometric optics approximation in which backscattering occurs from quasispecular surface points [Ishimaru, 1978; Ulaby et al., 1982].

The scalar approximation to physical optics uses a small slope assumption to further simplify the vector equations from the tangent plane approximation in the electromagnetic case to scalar equations [Ulaby et al., 1982; Eom, 1982]. The result is a cross section approximation with a relatively simple polarization dependence for application in cases where surface heights may not be large compared with the wavelength. The model predicts no cross-polarized backscattering. Kim et al. [1985] give a (misprinted) formula derived by Eom [1982] (where it is given correctly) for HH and VV cross sections in the scalar physical optics approximation, assuming an exponential form for the surface height correlation function:

$$\sigma^0_{pp} = 2\,|R_{pp}|^2 \cos^2\theta \exp\left(-k^2 h^2 \cos^2\theta\right) \times \sum_{n=1}^{\infty} \frac{\left(4k^2h^2\cos^2\theta\right)^n}{n!} \frac{k^2(n/L)}{\left(4k^2\sin^2\theta + n^2/L^2\right)^{3/2}} \tag{8}$$

where k is the free space wave number of the incident radiation, h is the standard deviation of rough surface height, L is the surface roughness correlation length, and R_{pp} is the Fresnel reflection coefficient (for the field, not the power) of the dielectric scattering material; the horizontal polarization reflection coefficient is to be chosen for R_{pp} when the pp = HH-polarized backscattering cross section is to be computed, and the vertical polarization reflection coefficient chosen for VV-polarized cross sections. Most dielectrics of interest in remote sensing display a Brewster angle in reflection; thus the reflection coefficient for horizontal polarization typically exceeds that for vertical polarization over a broad range of incidence angles. Consequently, the HH-polarized cross sections predicted by Equation (8) are often higher than their VV-polarized counterparts. This feature of this model is somewhat unusual and controversial.

8.2.3.2. Conventional Perturbation Theory. The treatment of rough surface scattering as scattering from a perturbed flat surface was first given by Rice [1951]. The theory has since been derived in alternate ways, but always with identical results [Ulaby et al., 1982; Tsang et al., 1985; Jackson et al., 1988]. The essential idea is to expand unknown scattered and transmitted fields in perturbation series with kh as the small parameter, where k is the radiation wave number and h is the standard deviation of surface heights. The dielectrics separated by the rough interface are assumed to extend to infinity both above and below. Expanding the boundary conditions in powers of kh allows an iterative solution of the perturbation equations, order by order. Ishimaru [1978] gives a convenient summary of results for the case of a dielectric with relative permittivity ε_r bounded above by free space. The first-order, or so-called Bragg scattering, backscattering cross sections for transmit and receive polarizations i and j are given by

$$\sigma^0_{ij} = 16\pi k^4 \cos^4\theta \; |\alpha_{ij}(\theta)|^2 \, W(2k \sin\theta, 0) \tag{9}$$

where θ is the angle of incidence, W is the power spectrum of surface roughness defined by the correlation function of surface heights $\rho(x, y) = \langle f(x_0 + x, y_0 + y) f(x_0, y_0) \rangle$,

$$W(K_x, K_y) = (2\pi)^{-2} \int_{-\infty}^{\infty} \int dx\, dy \exp\left(-iK_x x - iK_y y\right) \rho(x, y) \tag{10}$$

(we have for simplicity chosen the coordinate system such that the plane of incidence coincides with the x-z plane), and where

$$\alpha_{HH}(\theta) = \frac{\varepsilon_r - 1}{\left[\cos\theta + \left(\varepsilon_r - \sin^2\theta\right)^{1/2}\right]^2} = -R_h(\theta) \tag{11a}$$

$$\alpha_{VV}(\theta) = \frac{(\varepsilon_r - 1)\left[(\varepsilon_r - 1)\sin^2\theta + \varepsilon_r\right]}{\left[\varepsilon_r \cos\theta + \left(\varepsilon_r - \sin^2\theta\right)^{1/2}\right]^2} \tag{11b}$$

$$\alpha_{HV}(\theta) = \alpha_{VH}(\theta) = 0 \tag{11c}$$

There are several things to note here. First-order perturbation theory, like the physical optics model above, predicts no cross-polarized backscattering; cross-polarized backscattering appears in conventional perturbation theory as a second-order effect. Second, note that for any ε_r having a real part greater than one, VV-polarized backscattering will exceed that at HH-polarization, contrary to the situation in the model above. Finally, R_h in Equation (11a) is the Fresnel reflection coefficient for the field reflected from a flat interface between free space and the dielectric material beneath the rough interface.

Conventional, lowest order perturbation theory is generally accurate to within about 2 dB for surfaces with standard deviations of surface height less than 10% of the radiation wavelength, though very high surface slopes also degrade the accuracy of this approximation [Thorsos and Jackson, 1991]. The sensitivities of first-order cross sections to variations in ice permittivity and surface roughness statistics are discussed by Winebrenner et al. [1989].

8.2.3.3. Integral equation method. Fung and Pan [1987a, b] have developed an analytical model for electromagnetic scattering from perfectly conducting rough surfaces, named the integral equation method. This method has recently been extended by Fung et al. [1991] to treat rough interfaces between dielectrics. Thorsos [1988] has developed a numerical, Monte Carlo simulation method for the study of rough surface scattering, which he has also called the integral equation method. We employ in this chapter the method of Fung and coworkers, and thus in this context there is no opportunity for confusion. However, readers surveying the field of rough surface scattering more broadly should take care to avoid confusion of these two very different methods.

As we have noted, the fundamental problem in rough surface scattering is accurate approximation of the densities of Huygens' wavelet sources induced on the rough surface by the illuminating wave. The method of Fung and Pan [1987a, b] begins with an exact integral equation for the unknown source density (in this case, the surface current) on a given realization from an ensemble of rough surfaces. The zeroth-order solution to this equation is just the tangent-plane approximation for the source density. Fung and Pan iterate this equation once to produce an improved approximation (which is, roughly speaking, correct to higher order in surface curvature than the tangent-plane approximation [Dashen and Wurmser, 1991]). In the case where surface slopes are large, this improved approximation requires shadowing corrections to provide correct results [Ishimaru et al., 1991; Jin and Lax, 1990; Chen and Fung, 1990]. Thorsos and Jackson [1991] have argued further that this approach requires shadowing to limit long-range surface interactions and prevent divergent integrals in expressions for cross sections. However, in the case of moderate slopes and surface heights, Fung and Pan [1987a] derive like- and cross-polarized cross sections in terms of convergent integrals without explicit shadowing. They argue that convergence of the integrals results from the finite correlation length of surface roughness. Shadowing in this approach is applied as a correction to the final cross section results; the application is similar to that often made in classical physical optics theory [Ulaby et al., 1982]. The results agree with physical optics and perturbation theory in appropriate limits and compare favorably with numerical simulations for two-dimensional scattering problems by Chen et al. [1989] and data from controlled experiments [Fung and Pan, 1987a]. Thus, despite the disagreement between authors over the role of shadowing, there is evidence for the validity of numerical results from this method.

The extension of the Integral Equation Method by Fung et al. [1991] to the case of a general dielectric interface requires a similar treatment of two coupled integral equations but yields analogous results. In both our case studies, the integral equation method has been used to derive rough surface boundary conditions for the dense medium (volume scattering) theory (Section 8.2.2.4), and is always used in conjunction with this theory. Characterization requirements for surface roughness in this model are identical to those for the classical models described above.

8.3 CASE STUDY 1: A THIN GRAY ICE SHEET

8.3.1 Ice History and Characterization

Our first case study concerns a thin, snow-free gray ice sheet grown as part of the 1988 CRRELEX experiment at the Cold Regions Research and Engineering Laboratory in Hanover, New Hampshire (Chapter 9). The sheet began on the night of January 11–12, 1988, as a snow-nucleated ice sheet growing in a pond of simulated seawater with salinity of 24‰. (Pond salinity is purposely set lower than that of natural seawater so that CRRELEX ice sheet salinities approximate natural values despite New Hampshire winter temperatures warmer than those in the Arctic.) The sheet at first grew slowly in temperatures near freezing, and even experienced a small amount of melting during its first two days. A change to clear, cold weather on January 13 caused the sheet to begin growing rapidly. A trace of snow blew onto the sheet on the night of the 13th, giving the ice surface a very fine scale gravelly visual texture, though the surface relief measured less than 1 mm. By the morning of the 14th, the sheet was approximately 6.5 cm thick and a band of crystals resembling frost flowers covered the center of the sheet (Figure 8-2). The night of the 14th was clear and cold with air temperatures below –28°C. The backscattering and emission measurements for this study were acquired between approximately 1630 and 2330 EST, on the night of the 14th. Grenfell and Winebrenner report ice thickness measurements of 8.0 and 8.3 cm at 1630 and 8.3 cm at 2130. Onstott reports a thickness measurement of 7.5 cm at 1910. Our experience indicates the variation in these measurements was likely due to spatial variability in the ice sheet thickness. The frost-flower-like crystals persisted on the ice sheet through the morning of the 15th; various investigators reported ice thicknesses ranging from 11.5 to 12.4 cm by 1030 that morning.

Perovich measured temperature and salinity profiles on the mornings of January 14 and 15. Figure 8-3 shows the measured temperature and salinity profiles; the salinities from the morning of January 14 are averages of two measurements made at opposite ends of the pond. Note that the cold night of the 14th evidently caused upward brine extrusion. The salinity in the top centimeter of ice increased

Fig. 8-2. Eight-centimeter thick gray ice in the CRRELEX pond used for the first case study. Detailed characterization is reported in Section 8.3.1.

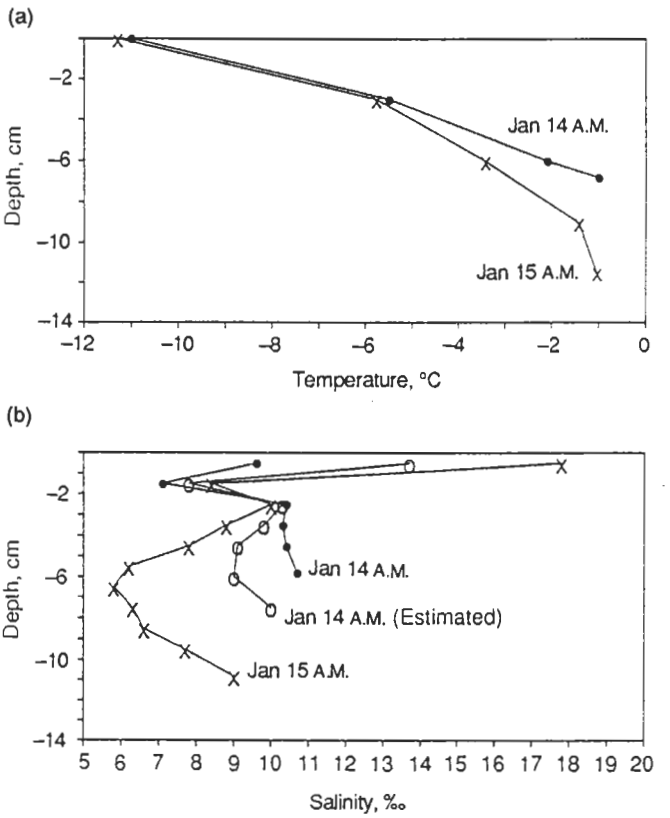

Fig. 8-3. (a) Temperature and (b) salinity versus depth in the gray ice sheet on the mornings of January 14 and 15 during CRRELEX in 1988. Grenfell and Winebrenner have heuristically estimated the salinity profile shown for late in the evening of January 14.

considerably, and salinity at depths 1 to 2 cm increased moderately; ice below 3 cm depth actually decreased in salinity. Ice temperature profiles were nearly linear on the 14th and 15th, except for the lowest point on the 15th which may be a temperature from a thermocouple in the water. We have no salinity profile for the night of January 14, i.e., at the time of the scattering and emission measurements. Grenfell and Winebrenner have therefore estimated the salinity profile at approximately 2000 on January 14 heuristically, with the result shown in Figure 8-3(b). We believe that more accurate salinity profiles than these would be difficult to acquire, given the horizontal variability in profiles at differing pond locations observed by Perovich and in nature by Tucker et al. [1984]. Reexamination of this issue may be necessary, however, if some signatures are conclusively shown to depend sensitively on details of this profile (Section 8.3.2.1). The ice surface temperature at the time of signature measurements was –16°C; we therefore estimate a linear temperature profile with this value at the air–ice interface and a temperature of –1°C at the ice–water interface.

Perovich acquired a horizontal thin section photograph of the ice at a depth of approximately 6 cm on the morning of the 15th, which unfortunately lacked sufficient contrast to estimate the permittivity correlation length using the method of Perovich and Gow [1991]. However, a reasonable estimate of the permittivity correlation length is possible based on an examination of ice morphology and comparison with data from other CRRELEX ice sheets with similar histories, temperatures, and salinities. Perovich estimates the permittivity correlation length in our sample to have been 0.15 mm. Perovich and Gow [1991] show that estimates of this correlation length display a typical random variation of about 30% for different horizontal locations within a macroscopically homogeneous ice sheet. Variations in depth and temperature lead to larger but more predictable correlation length variations.

Estimates of the air–ice interface roughness for this sheet are available from photographs of an ice sample removed by Onstott during the day on the 14th. The sample was stored at low temperature (≈–20°C) and later sectioned and photographed against a calibrated grid. The photo-

graphs were analyzed by two separate groups of investigators (by Bredow and Gogineni, and by Onstott) to derive independent estimates of surface roughness parameters. Both sets of estimates assume an exponential form for the correlation function of surface heights, $\rho(x) = h^2 \exp(-x/L)$, where x is spatial lag, and h is the standard deviation of surface height. Bredow and Gogineni [1990] estimate $h = 0.03 \pm 0.01$ cm and $L = 1.77$ cm with 90% confidence limits of 0.81 cm and 2.49 cm. Onstott estimates $h = 0.048$ cm and $L = 0.669$ cm. We have no information on under-ice surface roughness except a qualitative report by Onstott that the dendrite structure seemed uniform and displayed no obvious roughness on horizontal scales larger than the platelet size (which was less than 1 mm). We have no characterization of the frost-flower-like crystal aggregates appearing in the photograph in Figure 8-2.

Onstott acquired backscattering cross section measurements at 5.25 and 9.6 GHz for HH-, VV-, and cross-polarizations. He estimates the range of uncertainty to extend from 4 dB below to 2.6 dB above each data point. Overall, backscattering from this thin gray ice is weak. Co-polarized cross sections increase between 5 and 10 GHz whereas cross-polarized cross sections change relatively little.

Grenfell and Winebrenner acquired calibrated brightness temperatures for V- and H-polarizations over a range of incidence angles from 30° to 70° at frequencies of 6.7, 10, 18.7, 37, and 90 GHz. These brightness temperatures have been reduced to effective emissivities based on the measured ice surface temperature and sky brightness at each frequency. This facilitates the comparison of models that compute only emissivity with the data and with models that predict brightness temperature; outputs from the latter models are normalized exactly as are the observations. Grenfell estimates an accuracy of 0.02 in horizontally polarized emissivity and 0.01 for vertical polarization. The observed emissivities are generally high, especially at V-polarization. (Note that the H-polarization emissivity reported at 70° for 37 GHz is evidently contaminated by emission from the edge of the pond or some other structure.) A striking feature in these observations is the minimum in emissivity at 10 GHz, relative to 6.7 and 18.7 GHz, at both polarizations. The H-polarization emissivity at 50° incidence angle drops from 0.79 at 6.7 GHz to 0.70 at 10 GHz (a variation of 12%) before rising back to 0.77 at 18.7 GHz. While the corresponding variation at V-polarization is only 3%, this is still larger than the estimated measurement uncertainty. Data sets acquired before and after this data set show a similar anomaly, but data taken after alteration of the ice surface late on the 15th show no such feature. Data acquired earlier on the 14th by the University of Massachusetts Stepped Frequency Microwave Radiometer show a decreasing emissivity with increasing frequency between 4 and 7 GHz (K. St. Germain and C. Swift, personal communication). Grenfell has observed similar features in other CRRELEX ice sheets as well. Thus all indications are that the radiometers were functioning properly and the 10 GHz passive signature feature in these data is real.

8.3.2 Model Comparisons

8.3.2.1. Many layer strong fluctuation theory. The application of many layer SFT in this case is based on an eight-layer physical model for the ice. Temperatures and salinities are constant within each layer but vary with depth. The layers are of equal thickness (1 cm) and centered on the depth points in the estimated salinity profile for the night of January 14, except for the layer adjacent to the ice–water interface. Temperatures and salinities in each layer are set equal to the values of the estimated profiles at the centers of each layer, except for the layer adjacent to the air–ice interface. The thickness of the lowest layer and salinity of the uppermost layer were varied to examine model sensitivities to these poorly known parameters.

The model also requires assumptions about parameters such as brine pocket size and spacing, ice and brine permittivities (as functions of temperature), air bubble and ice crystal sizes, and mean brine pocket tilt and elongation. Although brine pockets are tilted from the vertical, their azimuthal orientations are random and uniformly distributed; thus the ice in this model possesses no macroscopic azimuthal anisotropy. Each of these parameters was set to the values used by Stogryn [1987] in his study of extinction, except for the values of mean brine pocket tilt and elongation. In the latter two cases, values suggested by previous characterization studies of artificial sea ice in CRRELEX [Arcone et al., 1986; Lin et al., 1988] were used. Specifically, these values are 4° for the mean brine pocket tilt (from vertical) and 10 for the ratio of brine pocket length to width (versus a tilt of 24° and ratio of 200 used by Stogryn). These parameters are assumed not to vary with depth in the ice sheet.

Figure 8-4 compares observations and signatures computed using two versions of the above physical model for the ice. Figure 8-4(a) shows computed and observed (effective) emissivities at 50° incidence angle, plotted versus frequency for V- and H-polarizations. One physical model is based on a total ice thickness of 8.3 cm, i.e., a lowest layer thickness of 1.3 cm, with layer salinities fixed at precisely those values specified by the estimated salinity profile. The uppermost layer salinity is 14‰ and results based on this model are labeled "8.3 cm, 14‰." An alternate model with total ice thickness 8.0 cm but an uppermost layer salinity of 20‰ is labeled "8.0 cm, 20‰." Both models show lower H-polarized emissivities at 10 GHz than at neighboring frequencies, though the feature is not quite as deep as that observed. The 8.3 cm model predicts an H-polarized 10 GHz emissivity of 0.74, whereas that observed is 0.70. The 8.0 cm model predicts 0.72, but agrees less well with the 6.7 GHz observation. Only the 8.0 cm model displays a feature at V-polarization, and this is also less pronounced than that in the data (0.96 predicted versus 0.93 observed). The predicted feature is an interference fringe caused by coherent interaction between field contributions from dif-

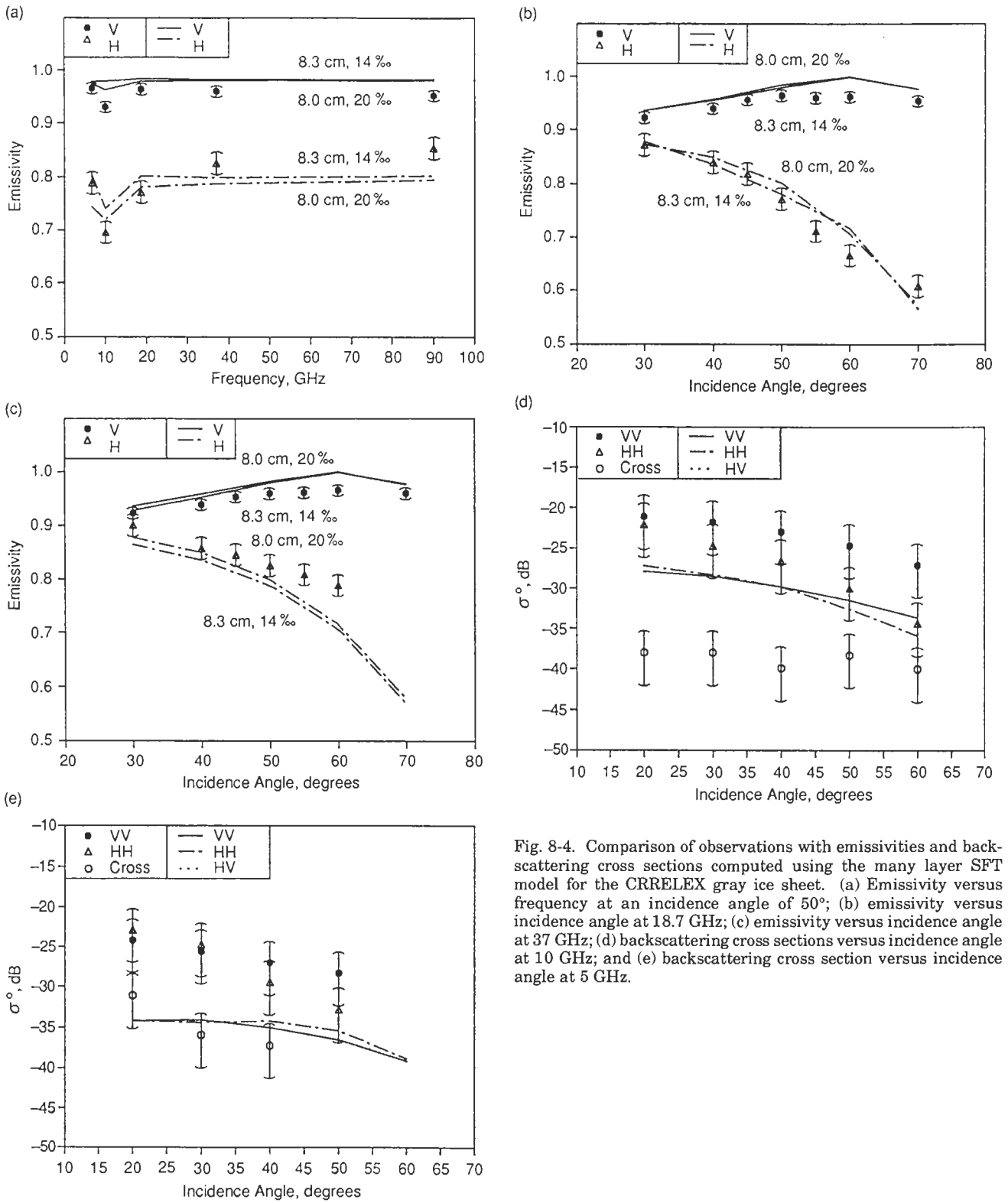

Fig. 8-4. Comparison of observations with emissivities and backscattering cross sections computed using the many layer SFT model for the CRRELEX gray ice sheet. (a) Emissivity versus frequency at an incidence angle of 50°; (b) emissivity versus incidence angle at 18.7 GHz; (c) emissivity versus incidence angle at 37 GHz; (d) backscattering cross sections versus incidence angle at 10 GHz; and (e) backscattering cross section versus incidence angle at 5 GHz.

ferent layers within the ice. Model emissivities vary almost precisely with the computed reflection coefficients; thus the model predicts virtually no effect of volume scattering on any of the passive signatures, but rather emissivity variations due solely to variations in the reflectivity of the stack of layers comprising the ice. The reflectivity variations are due to variations in the salinity, and therefore effective permittivity, profile of the ice sheet; there is nothing in the frequency dependence of other dielectric properties (brine permittivity, etc.) sufficient to produce such a large variation.

The predicted emissivity minimum is robust in that it occurs between 5 and 12 GHz for much wider variations in lower layer thickness and surface salinity than we have shown here. However, the exact location (i.e., frequency) and depth of the minimum are sensitive to those parameters. For example, an 8.0 cm model with 14‰ surface salinity produces a minimum emissivity closer to 6.7 GHz. Adding a tenuous but uniform snow layer atop the ice, in an attempt to model the frost-flower-like layer, leads to alterations in the fringe that depend sensitively on snow depth and density. Neglecting the salinity profile entirely leads to unrealistic results; emissivities computed from any single-layer model oscillate, as functions of frequency and incidence angle, much more than is observed. Thus according to this model, coherent effects are essential in explaining the observed feature, but details of the feature depend sensitively on thickness, near-surface salinity, and perhaps other details of the salinity and temperature profiles. Different growth histories (thus, differing salinity profiles) and changes to the near-surface salinity profile by a frost-flower layer would therefore alter the fringe predicted by many layer SFT, but would not eliminate the feature. The model also displays a milder sensitivity to the values chosen for mean brine pocket tilt and elongation. The values we use for these parameters lead to less predicted absorption and thus to slightly stronger coherent interaction effects than do those values used by Stogryn [1987]. Figures 8-4(b) and (c) show computed and observed emissivities versus incidence angle 18.7 and 37 GHz, respectively, for each of the two physical models. Penetration depths are much reduced at these frequencies, making the near-surface salinity the most important parameter. Predicted signature sensitivities to upper-layer salinity are, however, relatively small for salinities in the range shown. Emissivity predictions at 50° differ from observations by less than 0.03 except for H-polarization at 37 GHz, where the predicted value is 0.04 too low. Agreement is better at smaller incidence angles but worse at larger angles, where Brewster-angle effects are more apparent in V-polarization predictions than in observations and H-polarization observations fall off less rapidly than predicted. Figure 8-4(a) shows this effect worsens at 90 GHz. Finally, Figures 8-4(d) and (e) show like- and cross-polarized backscattering cross sections at 5 and 10 GHz, respectively, as functions of incidence angle. Model results are shown only for the 8.3 cm case because sensitivities are modest, on the order of those for 18.7 and 37 GHz emissivities. The many layer SFT model predicts volume scattering levels too low to explain the observed level of backscattering, at least with the present set of assumptions for brine pocket and other parameters. Note that predicted like-polarized cross sections show a different polarization behavior than indicated by the observations. Predicted cross-polarized cross sections fall below –55 dB.

8.3.2.2. Polarimetric strong fluctuation theory. Polarimetric SFT model results for this case are based on a physical model consisting of a single ice layer overlying seawater. Physical properties do not vary within the ice layer; thus an effective layer temperature and salinity, resulting in a brine volume of 4.2%, characterize the layer. The layer thickness is fixed at 8.0 cm. The permittivities of the ice background, brine inclusions, and underlying seawater are frequency dependent and specified in Table 8-1. The only remaining physical model parameters are the permittivity correlation lengths, Equation (7). These are set at l_x = 0.70 mm, l_y = 0.26 mm, and l_z = 1.2 mm, independent of frequency, incidence angle, or any other parameters. The correlation lengths were chosen to match model results with backscattering observations at 5 GHz and then fixed for all subsequent model calculations. They are consistent with values used previously in comparisons of this model with 9 GHz backscattering data for first-year ice near Point Barrow, Alaska [Nghiem, 1991]. Though we have no independent estimate of l_z in this case study, the value of l_z is comparable to values found in another study of artificial sea ice in CRRELEX [Arcone et al., 1986; Lin et al., 1988]. The values of l_y and l_x are notably larger than Perovich's correlation length estimate (consistent with the reasoning in Section 8.2.2.6).

Figure 8-5 compares the computed signatures with backscattering and emission observations. Figure 8-5(a) is a plot of emissivities versus frequency at 50° incidence angle. Model emissivities agree with observations to within 0.025, except at 10 GHz (and at 90 GHz, where results are not available). V-polarized model results are 0.05 higher than experiment at 10 GHz, while at H-polarization the difference is 0.10. Angular emissivity responses at 18.7 and 37 GHz are shown in Figures 8-5(b) and (c). Although the differences between theory and experiment are similar to those in many layer SFT, the quantitative agreement here is better for 37 GHz, H-polarization. Passive signature results are insensitive to the choice of correlation length, indicating a minor role for scattering in this model for passive signatures. Ice sheet reflectivities, determined by the mean permittivity, govern the computed emissivities. The 6.7 GHz emissivities display a modest sensitivity to layer thickness. Because dielectric absorption is higher in the vertical direction (Table 8-1), this sensitivity is greater for horizontal than for vertical polarization.

Figures 8-5(d) and (e) compare observations with model predictions for like- and cross-polarized backscattering cross sections versus incidence angle, at 5 and 10 GHz, respectively. Theory for the 5 GHz, like-polarization cross

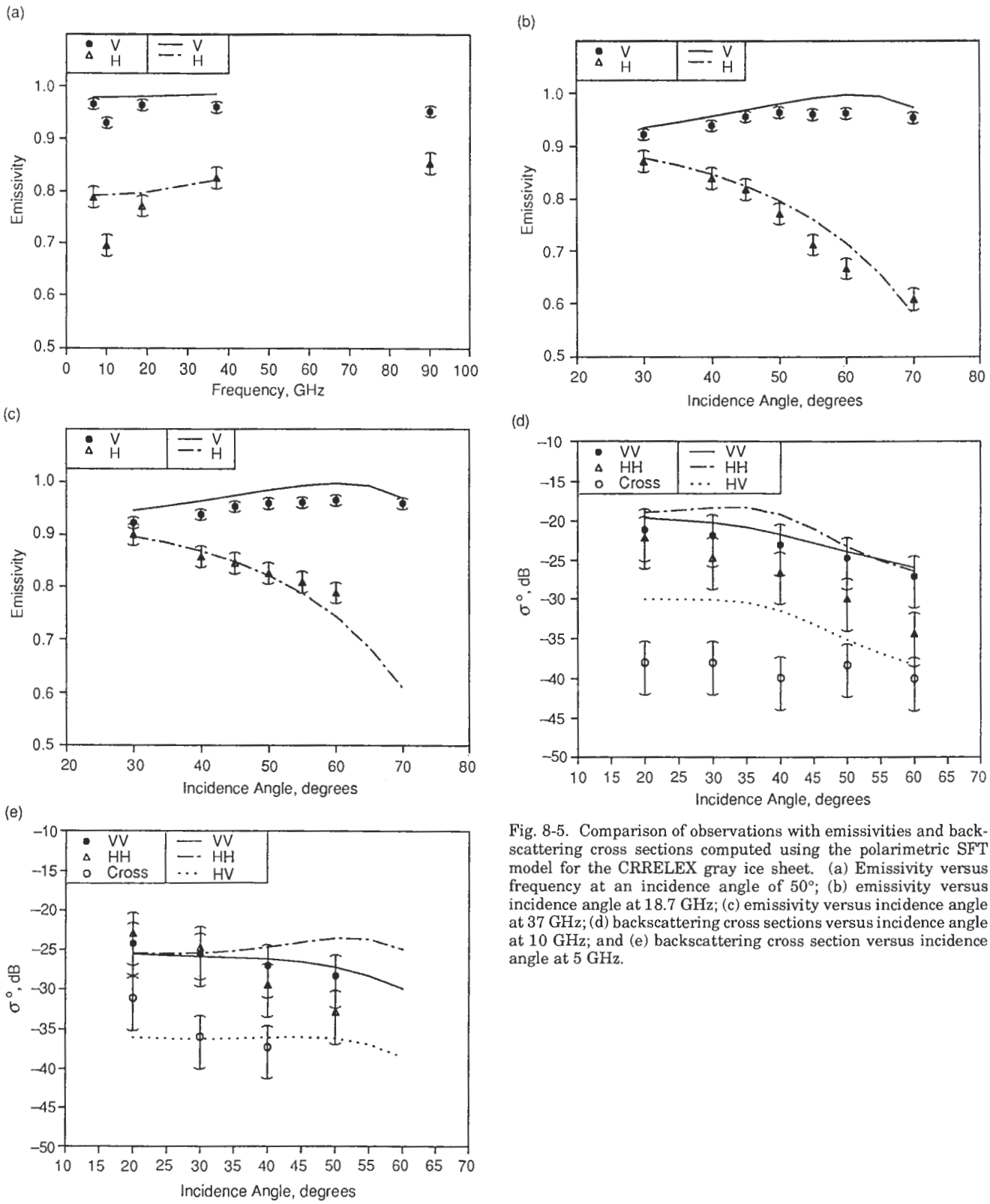

Fig. 8-5. Comparison of observations with emissivities and backscattering cross sections computed using the polarimetric SFT model for the CRRELEX gray ice sheet. (a) Emissivity versus frequency at an incidence angle of 50°; (b) emissivity versus incidence angle at 18.7 GHz; (c) emissivity versus incidence angle at 37 GHz; (d) backscattering cross sections versus incidence angle at 10 GHz; and (e) backscattering cross section versus incidence angle at 5 GHz.

TABLE 8-1. Relative permittivities of materials in the Polarimetric SFT Model for the CRRELEX gray ice sheet.

Frequency, GHz	Seawater	Background ice	Brine inclusions	ε_{eff}	ε_{effz}
5.0	60 + i34	3.15 + i0.0015	37.5 +i43.1	3.53 + i0.072	4.10 + i0.40
6.7	60 + i34	3.15 + i0.0015	32.1 +i38.6	3.53 + i0.086	4.06 + i0.459
10.0	42 + i34	3.15 + i0.0015	24.0 + i32.0	3.51 + i0.116	3.92 + i0.562
18.7	30 + i34	3.15 + i0.0025	14.0 + i21.0	3.44 + i0.187	3.53 + i0.675
37.0	10 + i20	2.92 + i0.0030	9.8 + i12.0	3.07 + i0.182	2.92 + i0.433

sections agrees with observations to within better than 3 dB at 20° and 30°; the agreement is similar for cross-polarization at 30° and 40°. However, the model predicts HH-polarized backscattering higher than observations at larger incidence angles and a difference between HH- and VV-polarizations opposite to that observed. Model predictions at 10 GHz are 1.5 to 10 dB above the observations for incidence angles less than 50°, and the predicted like-polarization difference is again opposite to that observed. The predicted cross-polarized cross sections also exceed observed levels. The increased discrepancy at 10 GHz may result in part because permittivity correlation lengths were set on the basis of results at 5 GHz (see above). However, setting correlation lengths based on results at 10 GHz yielded less satisfactory results overall. In contrast to model predictions for emission, backscattering cross sections are sensitive to the scatterer size parameters, i.e., to the permittivity correlation lengths. The 5 and 10 GHz cross sections display a comparable or greater sensitivity to thickness of the ice layer as well; the backscattering level, frequency response, and VV-HH polarization contrast are all sensitive to this parameter.

8.3.2.3 Modified radiative transfer. The equations of modified radiative transfer have at present been solved only for a single, infinitely thick scattering layer. Thus the MRT results presented here are based on a physical model for the ice in which the ice–water interface plays no role and ice properties do not vary with depth. Dielectric properties are modeled as directionally anisotropic, however, with a specified tilt direction for the (single) preferred direction (i.e., the optic axis). Thus the tilt direction, as well as mean permittivities, normalized variances of permittivity (i.e., the variance divided by the mean squared) and permittivity correlation lengths, in directions parallel and perpendicular to the preferred direction, must be specified directly. Specification of these parameters was guided generally by knowledge of the ice structure and parameters, but detailed choices were based also on experience with this model. The parameters used to produce nearly all the results shown below are as follows. The preferred direction coincides with the vertical. This reflects the macroscopic azimuthal isotropy of the ice sheet, while accounting for the vertical elongation of brine pockets. The mean permittivities are then 3.3 + i0.1 perpendicular to the preferred direction (horizontal) and 3.4 + i0.16 parallel (vertical). The normalized variances are 0.1 horizontal, 0.2 vertical. Finally, the permittivity correlation lengths are set at 1 mm in the vertical (reflecting the vertical extent of brine pockets) and 0.1 mm in the horizontal (reflecting the horizontal extent). Some results for backscattering sections were computed with different parameters as well for the purpose of studying sensitivities. We give the additional parameters below.

Figure 8-6(a) compares emissivities computed using MRT above with observations as a function of frequency at 50° incidence angle. Recall that the present solution of MRT is only a first-order scattering solution. Predictions at V-polarization, with the exception of 10 GHz, show good agreement even at 90 GHz. The predictions predict no feature at all at 10 GHz, however. Figures 8-6(b) and (c) show emissivity predictions and observations versus incidence angle for 18.7 and 37 GHz, with particularly good agreement at 37 GHz, V-polarization. Figures 8-6(d) and (e) show backscattering cross sections at 10 GHz computed using two different sets of input parameters. Like-polarized cross sections computed from the parameters given above fall approximately 20 dB below the observations, though the predicted polarization contrast is in approximate agreement. The most sensitive parameters in computing backscattering cross sections are the imaginary parts of the mean permittivities and permittivity correlation length. Reducing the imaginary parts and increasing correlation lengths increases predicted backscattering to a level compatible with the observations, as shown by the results in Figure 8-6(e). The parameters used to compute the latter result are mean permittivity of 3.1 + i0.001 and correlation length 0.15 mm in the horizontal direction, and 3.2 + i0.002 and 0.2 mm in the vertical. Although the computed VV-HH contrast is smaller than that observed, it has the correct sign. Note, however, that this model produces no cross-polarized response; this is a characteristic of most first-order scattering models when the scattering

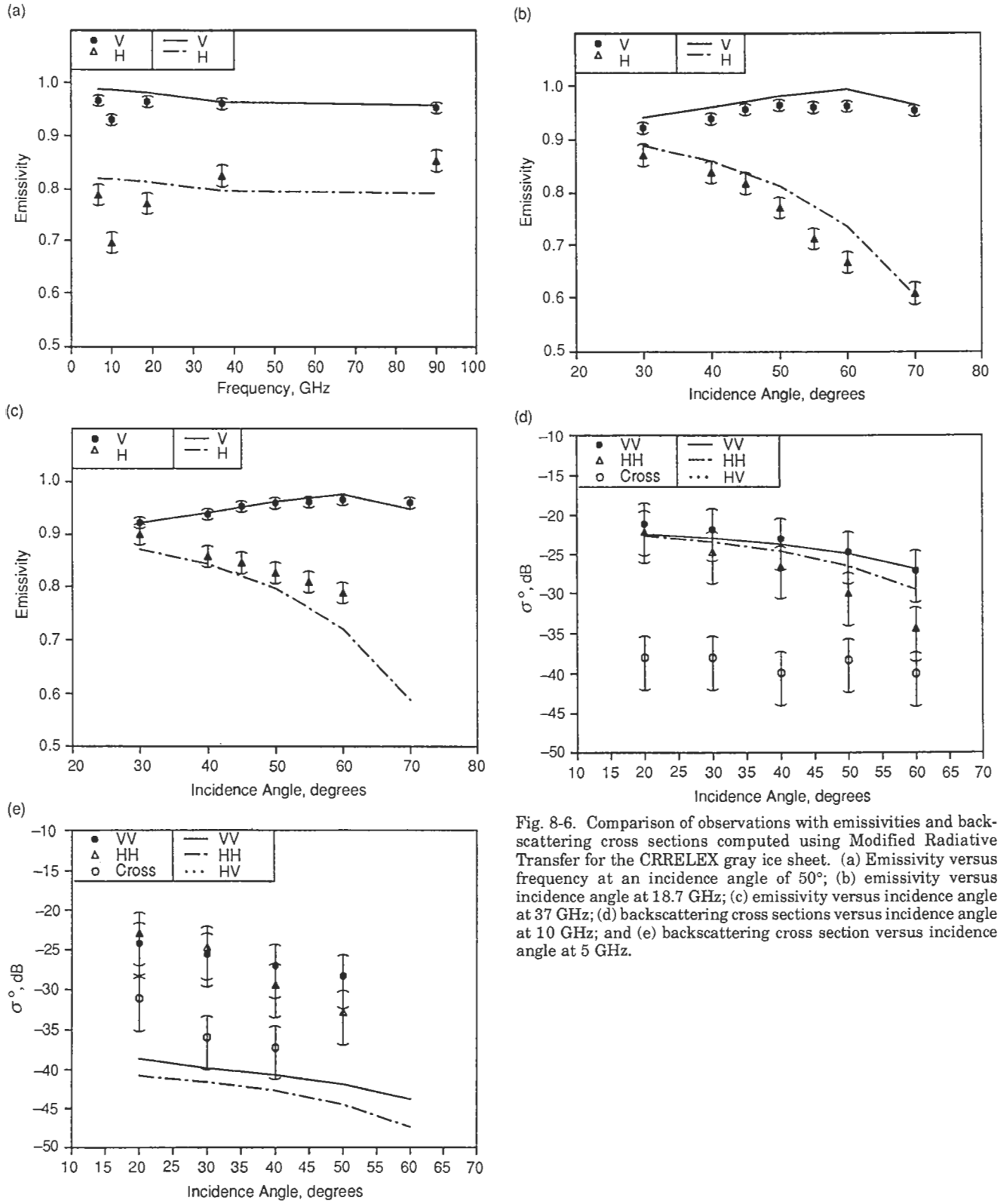

Fig. 8-6. Comparison of observations with emissivities and backscattering cross sections computed using Modified Radiative Transfer for the CRRELEX gray ice sheet. (a) Emissivity versus frequency at an incidence angle of 50°; (b) emissivity versus incidence angle at 18.7 GHz; (c) emissivity versus incidence angle at 37 GHz; (d) backscattering cross sections versus incidence angle at 10 GHz; and (e) backscattering cross section versus incidence angle at 5 GHz.

medium is azimuthally isotropic.

8.3.2.4. Physical optics under the scalar approximation. The model used by Drinkwater [1989, 1987] neglects volume scattering in high-density congelation ice. Thus the model reduces in this case to a purely surface scattering model based on physical optics under the scalar approximation. The model assumes that beneath the rough surface lies a directionally isotropic dielectric material with no depth variation. Thus the results below assume a physical model for the ice in which finite ice thickness and dielectric anisotropy play no role. The (scalar) permittivity of the ice must be computed in light of the penetration depth and temperatures and salinities over that depth. The permittivity is computed in this case using the model of Vant et al. [1978], assuming vertically oriented brine pockets 0.91 mm long and 0.15 mm wide. Ice temperature and salinity are set to the observed air–ice interface temperature of –16° and surface salinity of 14‰. Ice density is assumed to be 0.92 g/cm^3; the computed brine volume fraction is 5.4%. The resulting permittivities are 3.74 + i0.20 at 5 GHz and 3.66 + i0.23 at 10 GHz. The uncertainty in surface roughness statistics motivated computation of a range of model results based on the range of likely surface parameters.

Figure 8-7 shows observations and model predictions for like-polarized backscattering cross sections based on two sets of surface parameters. The first set of parameters, h = 0.02 cm, L = 2.49 cm (where L is the correlation length in the exponential correlation function of Section 8.3.1), correspond to the smoothest surface within the limits of uncertainty reported by Bredow and Gogineni [1990]. The second set of parameters, h = 0.048 cm, L = 0.669 cm, corresponds to the roughest surface consistent with the characterization data, namely that reported by Onstott. Figure 8-7(a) presents results at 10 GHz. (Recall that the physical optics model does not predict cross-polarized backscattering and that it treats backscattering only; it does not treat emission.) Using the roughest probable surface parameters, the predicted HH-polarized cross sections fall only 2–3 dB below the observations. This is encouraging given that the result relies only on independent characterization information. However, the polarization dependence is opposite to that observed; the predicted cross sections at VV-polarization fall below those for HH and well below the observations.

Figure 8-7(b) shows analogous results at 5 GHz. Here, the validity criteria for the model are rather severely violated (Section 8.2.3.1). The plot shows the best available fit to the observations using parameters within the range specified by independent characterization. Results at neither polarization compare well with observations.

8.3.2.5. Conventional perturbation theory. The probable roughness parameters are within the range where conventional perturbation theory should apply at 5 and 10 GHz. Figure 8-8 compares observations with results from first-order perturbation theory based on ice permittivities identical to those used in the physical optics model above.

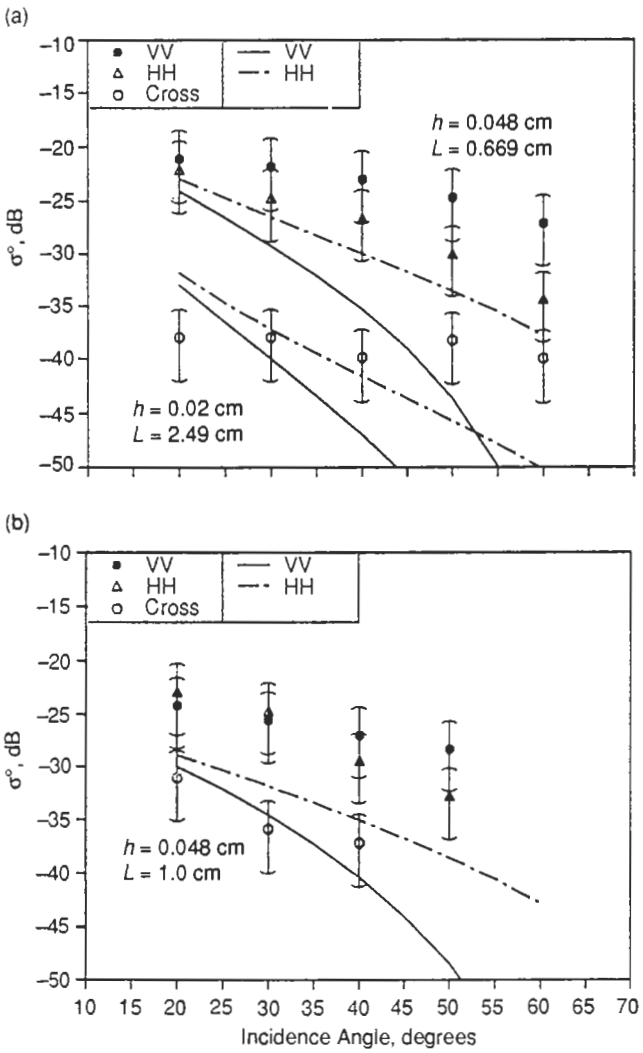

Fig. 8-7. Comparison of observations of the CRRELEX gray ice sheet with backscattering cross sections computed using the physical optics rough surface scattering model of Section 8.2.3.1 for backscattering cross sections versus incidence angle at (a) 10 and (b) 5 GHz.

Figure 8-8(a) shows the range of 10 GHz model predictions for the range of roughness parameters reported by Bredow and Gogineni [1990]. Using the upper limit of their height standard deviation and the shortest correlation length within their 90% confidence interval, model predictions are approximately 4 dB below the observations at 30° incidence angle for both polarizations; at 50° the figure is 6 dB. Model results for the roughness parameter values reported by Onstott, Figure 8-8(b), fall approximately 2.5 dB and 4 dB below the observations at 30° and 50°, respectively, for both polarizations. Thus the sign and magnitude of the VV-HH cross section difference predicted by this model agree well with the observations, but the overall level

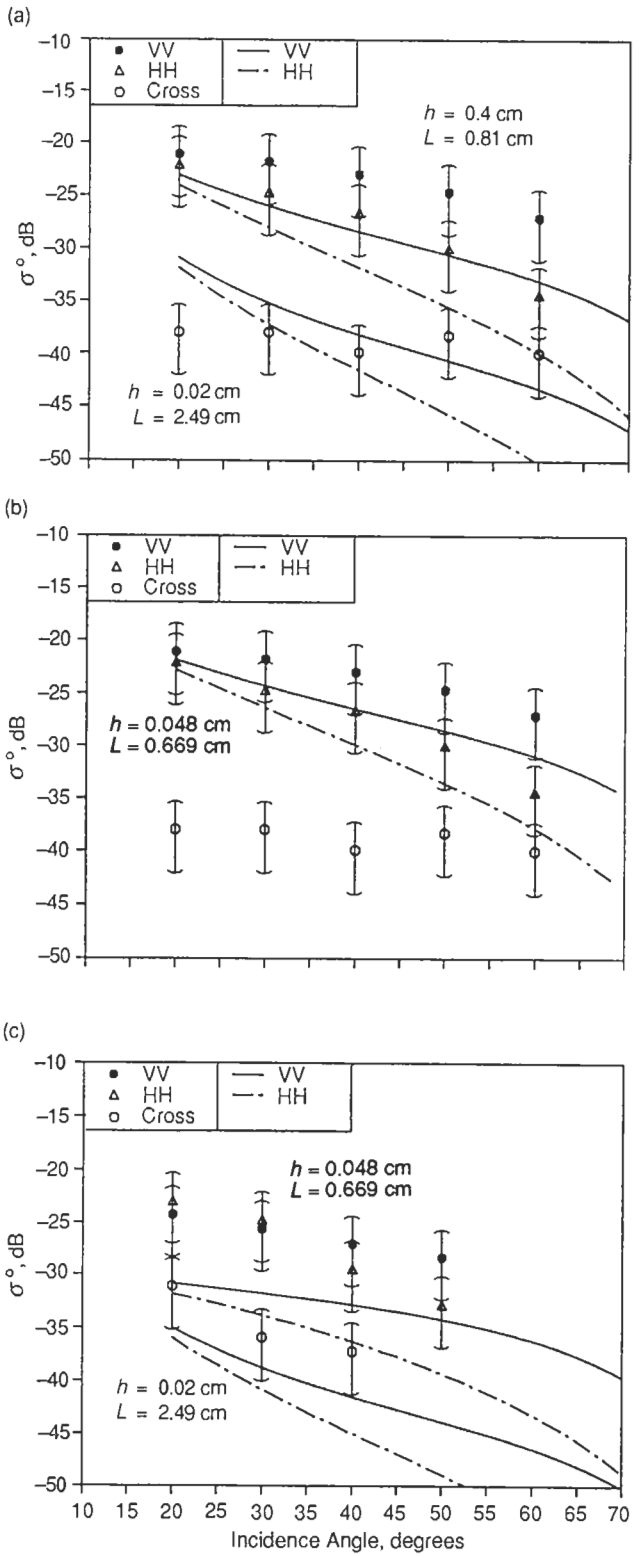

Fig. 8-8. Comparison of observations of the CRRELEX gray ice sheet with backscattering cross sections computed using conventional first-order perturbation theory. (a) and (b) Backscattering cross sections at 10 GHz for three sets of roughness parameters consistent with the reported measurements, and (c) backscattering cross sections at 5 GHz.

of backscattering is, at best, barely within the estimated uncertainties in the observations.

It is interesting to note that this comparison is not invalidated by the inference of finite-thickness effects from the many layer SFT model comparison. Recall that the first-order HH-polarized backscattering cross section is proportional to the power reflection coefficient, and that this result remains true even for layered media. The results above suggest that the power reflection coefficient of our CRRELEX '88 gray ice differs from that of infinitely thick ice by an amount on the order of 12 to 14%. This would alter the backscattering cross section of our gray ice sample by the same amount for HH-polarization. Yet here we find marginal agreement with results from an infinite-thickness model. This can be resolved by noting that backscattering cross sections are expressed in decibels, and the results for infinite thickness differ from those for finite thickness by less than 1 dB. Thus while 10 GHz passive signatures appear quite sensitive to finite thickness effects, 10 GHz backscattering is much less noticeably so.

At 5 GHz, the predicted VV-HH cross section differences again closely track the observations, but the predicted levels of backscattering are, at best, more than 6 dB too low. Figure 8-8(c) shows the range of possible results based on the independent roughness data. It appears that some physics other than, or in addition to, rough surface scattering from effectively infinitely thick ice must be involved in backscattering at 5 GHz.

8.3.2.6. Dense medium theory—integral equation method. The application of dense medium theory (DMT) in this case is based on a single-layer physical model for the ice, with constant ice properties within the layer and rough interfaces at both the top and bottom. The brine pockets are assumed spherical with radius 0.1 mm; brine volume is set at 5% based on the average temperature and salinity of the ice. The permittivities of the brine pockets and underlying seawater, as well as the computed mean ice permittivities, are given in Table 8-2. The depth of the layer is set at 7.5 cm. Roughness parameters for the air–ice interface are set at $h = 0.05$ cm and $L = 0.67$ cm. The corresponding parameters for the ice–water interface are $h = 0.03$ cm and $L = 0.96$ cm. The under-ice roughness parameters are plausible but constrained only loosely by Onstott's qualitative observation. Recall that DMT-IEM treats emission from nonisothermal layers; thus, in emission computations, a linear temperature profile is used assuming an ice–water interface temperature of –1°C and an air–ice interface temperature of –10°. The emitted brightness temperatures have been converted to effective emissivities here by dividing by the measured surface ice temperature, consistent with the reduction of the emission observations. Identical input parameters are used for all polarizations, frequencies, and incidence angles in both passive and active calculations.

Dense medium theory predicts only negligible volume scattering within the ice layer for these parameters. Thus

TABLE 8-2. Relative permittivities of materials in the Dense Medium–Integral Equation Model for the CRRELEX gray ice sheet.

Frequency, GHz	Seawater	Brine inclusions	ε_{eff}
6.7	60.4 + i39.4	50.4 + i40.3	3.40 + i0.19
10.0	35.0 + i38.0	33.5 + i38.7	3.35 + i0.17
18.7	18.4 + i30.2	18.4 + i28.2	3.30 + i0.16

predicted emissivities are dominated by emission from the lossy ice layer and backscattering results entirely from rough surface scattering at the upper and lower ice interfaces. Figure 8-9 compares observations with computed effective emissivities for 6.7 and 18.7 GHz (passive signatures at 37 GHz and other frequencies were not computed). Model results agree quite closely with H-polarization observations at 6.7 GHz, and do not show a strong sensitivity to thickness. Computed emissivities at 18.7 GHz are higher than the observations, but the angular trend for V-polarization shows no pronounced peak at large incidence angles, i.e., Brewster-angle effect. This trend, if not the actual predicted emissivities, is similar to that of the observations and notable among the models in this case study. V-polarized emissivities at 6.7 GHz, however, do show a strong Brewster-angle effect. The plot of computed emissivities versus frequency, Figure 8-9(c), does not show the 10 GHz feature present in the observations; though this plot contains model values at only 6.7 and 18.7 GHz, and thus could not show the feature, DMT does not predict such a feature in any case. Figures 8-9(d) and (e) show computed backscattering cross sections at 5 and 10 GHz, respectively. The 5 GHz results match the observations very closely. The predicted backscattering is due mostly to scattering at the ice–water interface. Although the assumed roughness at this interface is fairly small, the large dielectric contrast between ice and water causes scattering strong enough to dominate the overall response, even after accounting for absorption in the ice layer. Results at 10 GHz are computed using identical roughness parameters; these results agree with observations to within approximately 2.5 dB. In this case, scattering from the ice–water interfaces accounts for only about half the total; the rest is due to scattering at the air–ice interface.

8.3.3 Discussion

A few inferences seem reasonably firm, based on the model comparisons above. First, the thin, relatively saline gray ice in this study is not a strong scatterer. Passive signatures are dominantly influenced by the reflection properties of the ice; in none of the emission models does scattering play much of a role in determining the effective emissivity. Backscattering, which must be due entirely to scattering, is relatively weak; this gray ice sample clearly differs in some important way from the strongly backscattering gray ice mentioned in the introduction. Because backscattering is weak, it may be more likely that several weak processes combine to determine what we see.

Several of the present models compute effective emissivities for simple, gray congelation ice that agree with observations to within $\lesssim 0.05$, for both polarizations at 19 and 37 GHz, for incidence angles less than 55°. Both the strong fluctuation theory models, which include finite thickness effects, as well as the (effectively) infinite-thickness modified radiative transfer model achieve this accuracy, at least in our case. On the other hand, emissivities at the lower frequencies (6.7 and 10 GHz) evidently depend not only on ice thickness, but also on the profiles of ice temperature and salinity. We infer this because only many layer SFT treats coherent interactions between waves from several depths within the ice, and only this model reproduces even partly the emissivity feature we observe. However, the sensitivity of the present many layer SFT model may incorrectly imply a greater signature variability than we observe in nature. A partially coherent model, to account for the patchiness of frost flowers, irregularity of surface brine layers, and so on, may be necessary. We note also that none of our model results at 90 GHz show good agreement with observations, suggesting that essential physics remains unaccounted for at millimeter-wave frequencies.

The situation for backscattering depends strongly on frequency as well. At 10 GHz, rough surface scattering from the upper ice surface (assuming effectively infinite ice thickness) correctly predicts the observed difference in like-polarized cross sections, but the cross sections themselves are lower than the observations by amounts that increase with increasing incidence angle. Model predictions fall barely within the estimated range of uncertainty in the observations when we use the independently derived surface roughness parameters corresponding to the roughest surface. Thus surface scattering without finite thickness effects may explain the present observations, though the observations support such an explanation only marginally. As we have noted in Section 8.3.2.5, this result is consistent with the finite-thickness reflectivity variation at 10 GHz implied by the emissivity observations. It may also be interesting to note that using the same parameters in the Gaussian correlation function $\rho(x) = h^2 \exp[-x^2/L^2]$ produces results that agree with the observations to within 0.5 dB. This shift in the form of the correlation function is plausible given the present uncertainty in our roughness characterization, but the data cannot be said to motivate such a shift.

It seems much less likely that uncertainty in the surface roughness characterization can account for the differences between 5 GHz observations and predictions based on backscattering from the air–ice interface alone. While this mechanism again accurately predicts the difference between like-polarized backscattering cross sections, the pre-

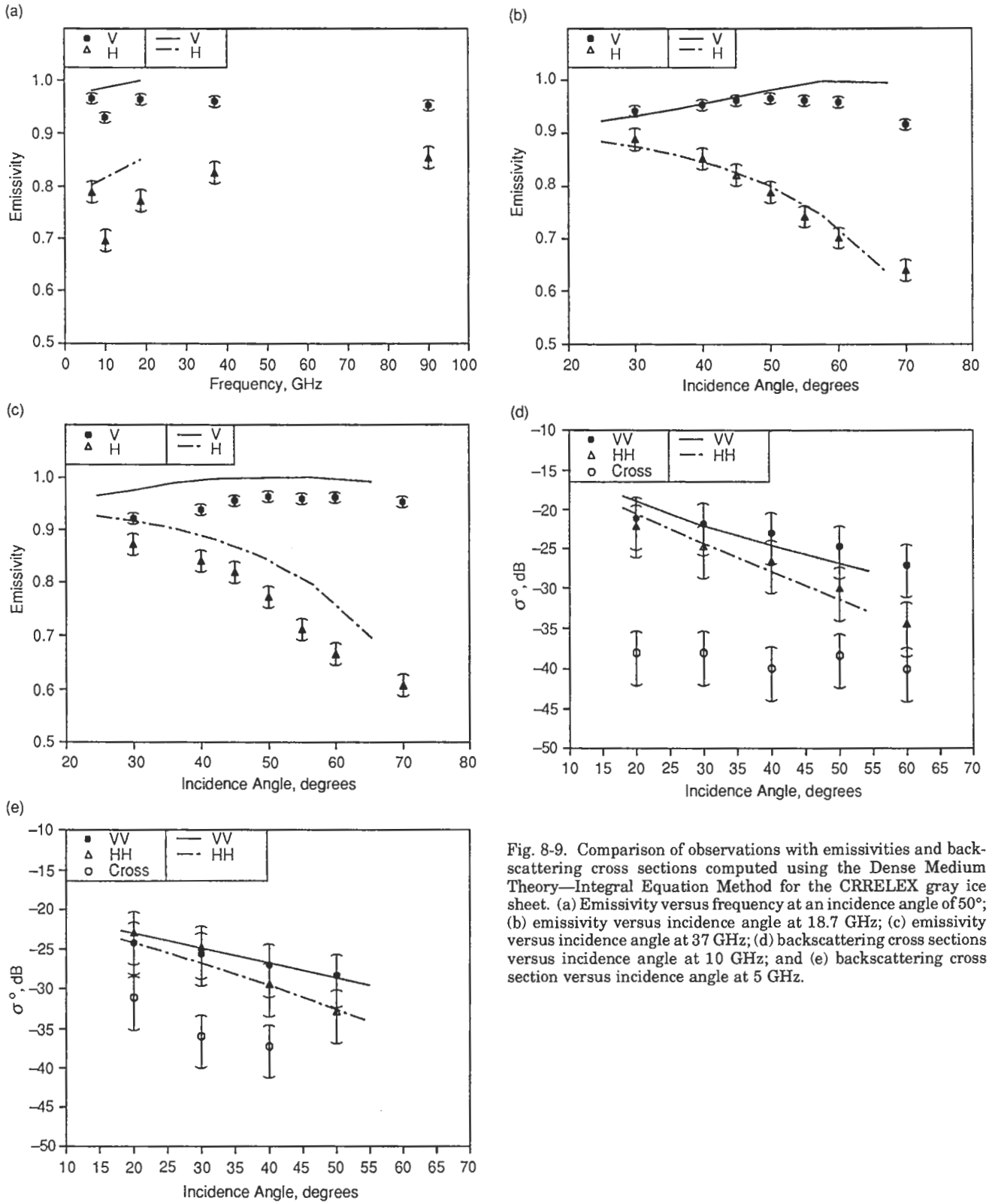

Fig. 8-9. Comparison of observations with emissivities and backscattering cross sections computed using the Dense Medium Theory—Integral Equation Method for the CRRELEX gray ice sheet. (a) Emissivity versus frequency at an incidence angle of 50°; (b) emissivity versus incidence angle at 18.7 GHz; (c) emissivity versus incidence angle at 37 GHz; (d) backscattering cross sections versus incidence angle at 10 GHz; and (e) backscattering cross section versus incidence angle at 5 GHz.

dicted level of backscattering is well below the observations. Our findings here are similar to those of Bredow and Gogineni [1990] based on C-band observations of this same ice sheet earlier on January 14. All of our models estimate penetration depths on the order of the ice thickness (8 cm) at 5 GHz (wavelength 6 cm). The combined Dense Medium Theory—Integral Equation Method provides a close match to 5 GHz observations based on rough surface scattering at the ice–water interface with plausible parameters. However, we have no quantitative information on under-ice roughness with which to test this explanation, nor do we have observations that could rule out other potential explanations. Examples of the latter might include scattering due to the patchiness of surface brine layers, volume scattering from larger scale inhomogeneities in the ice, or reflectivity variations due to depth variations in ice properties.

8.4 CASE STUDY 2: COLD OLD ICE

8.4.1 Ice Characterization

The data for this case study were acquired from October 3 through 8, 1988, as part of the CEAREX experiment in the Arctic Ocean, north of the Barents Sea. Air temperatures were –16 ±2°C and had been well below freezing for more than two weeks. Snow–ice interface temperatures were –10 ±2°C or less. The ice was completely frozen to depths (from the snow–ice interface) greater than 50 cm [Wettlaufer, 1991]. The old ice floe on which our observations were made seemed in no way remarkable compared with other old ice floes in the area, or in the experience of the investigators present.

The microwave signatures of old ice and the physical properties of its upper layers are both highly variable (Chapters 2, 4, and 5). Raised old ice areas typically display strong backscattering and low brightness temperatures, whereas nearly refrozen melt ponds are often characterized by relatively low backscattering and brightness temperatures similar to those of first-year ice. Very low-density, bubbly upper layers are common to raised areas, whereas refrozen melt ponds are typically much denser. There may be systematic differences in the salinities, roughnesses, and other properties of these two old ice types as well. We have therefore structured this as a dual case study, selecting two old ice sites from the same floe that apparently bracket the extremes of upper layer density as well as signature behavior. For each site, Grenfell acquired vertically and horizontally polarized brightness temperatures at 6.7, 10, 18.7, and 90 GHz, for a range of nadir angles from 30 to 70°. Data at 37 GHz were also acquired at the melt pond site. The data have been reduced using measured sky brightness temperatures and we have again normalized these data by the snow–ice interface temperature to produce effective emissivities, for the same reasons as in the previous case study. Nearly simultaneously with the passive data, Onstott acquired HH-, VV-, and cross-polarized backscattering cross sections at 10 GHz over a similar range of incidence angles.

Our first site is a raised area of ice known as drift station site 7 (abbreviated DS-7). The uppermost layers of ice at this site consisted of a fragile, geometrically complex matrix of air and ice containing many bubbles and some irregular, interconnected air spaces that we call voids. Beneath this matrix was a layer of ice that, while still bubbly, was more easily described in terms of discrete bubbles embedded in an ice background. Figure 8-10 shows a schematic drawing of ice structure versus depth, as well as profiles of ice salinity and density below 19 cm depth, based on analysis by Gow of a core sample taken from the site. Figure 8-10

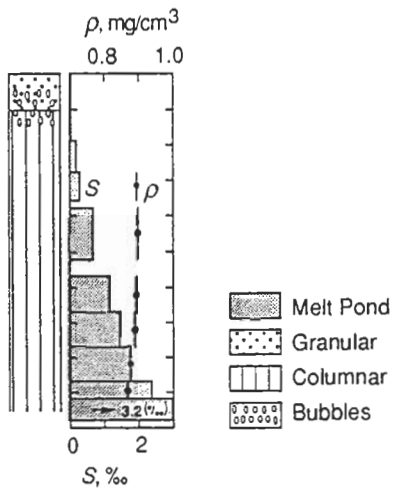

Snow: Layer Thickness = 10 cm
Consists of Platelets and Rimed Needles
Platelets 0.1 mm Thick and 0.5 mm Wide
Needles 0.1 to 0.2 mm Thick and 0.3 to 0.6 mm Long
Snow Density Approximately 0.1 gm/cm^3

Ice: Consists of a 19-cm Decomposed Layer Over Columnar Ice

Density Profile		Salinity Profile	
cm	ρ, mg/m^3	cm	‰
		0–19	0.0
19–66	0.895	19–28	0.1
66–77	0.89	28–36	0.3
77–87	0.88	36–38	Break in Core
87–92	0.87	38–53	0.7
		53–57	Break in Core
		57–67	1.2
		67–77	1.4
		77–87	1.9
		87–92	2.4
		92–98	3.0

Fig. 8-10. Structure, density and salinity in the upper ice layers at DS-7, numerical density and salinity profiles and snow cover observations.

also shows numerical salinity and density profiles, and semiquantitative observations by Grenfell of snow cover parameters at the site. Grenfell measured –19, –18, and –10°C for the air, air–snow interface, and snow–ice interface temperatures, respectively, with an estimated error in each case of ±2°.

Coring so badly disrupted the structure of the bubbly ice that quantitative parameters derived from the core cannot be considered reliable at depths less than 19 cm. To circumvent this problem, Onstott extracted larger samples of the upper ice layers using a chain saw. Based on these samples, he reports structure in the uppermost part of the ice consisting of two distinct layers, the first containing a great many bubbles as well as large voids, the second containing fewer, more discrete bubbles and fewer, smaller voids. Figures 8-11(a) and (b) each show two thick sections of each layer. Note that each photo is actually a juxtaposition of two separate photos, one of each layer against a calibrated background. The upper ice layer, in particular, is so riddled with inhomogeneities that it seems uncertain whether it can realistically be described in terms of discrete air bubbles, or even a size distribution of air bubbles, embedded in ice. Nonetheless, Onstott has visually derived mean bubble sizes, characteristic void dimensions, and layer thickness for each layer, and has measured bulk layer density, salinity, and snow–ice interface roughness as well. He reports a standard deviation for snow–ice interface roughness of $h = 0.14 \pm 0.02$ cm with a correlation length $L = 2.0 \pm 1.3$ cm—assuming, as in the previous case study, a correlation function of the form $\rho(x) = h^2 \exp(-x/L)$. The upper, most porous ice layer is 5.0 ±0.6 cm thick, with salinity 0.0‰ and density 0.457 g/cm^3. Mean bubble diameter was estimated to be 2.5 mm with a characteristic air void dimension of 8 mm. The lower, less porous layer is reported to be 3.5 ±0.4 cm thick. Salinity in this layer was also 0‰, but the density was 0.728 g/cm^3. Mean bubble diameter was 4 mm with a characteristic void dimension of 2 mm. Based on Onstott's and Gow's measurements, the ice density below 8.5 cm depth increased to 0.895 g/cm^3, nearly that of pure ice (0.917 g/cm^3). We do not have measurements of total ice thickness at DS-7. However, we know that thickness was greater than 1.5 m and that ice salinity increased below 1 m to approximately 3‰; thus the lower portions of the ice were electromagnetically lossy, and it is virtually certain that neither the lower ice surface or underlying seawater affected the observed signatures.

HH- and VV-polarized backscattering cross sections for this site differ little; both are high (generally between 0 and –5 dB) and almost independent of incidence angle. Cross-polarized backscattering is also strong (above –20 dB). Effective emissivities decline sharply with increasing frequency and show little polarization dependence. Thus it appears that scattering at this site is indeed quite strong.

Contrast this with our second site, a refrozen melt pond some tens of meters from DS-7, known as the Del Norte melt pond. Backscattering cross sections for this site are much lower than those at DS-7, whereas effective emissivities are considerably higher. Figure 8-12 shows a thick section photograph of a sample acquired at this location by Onstott. (Note that this photo is not a juxtaposition; it shows only a

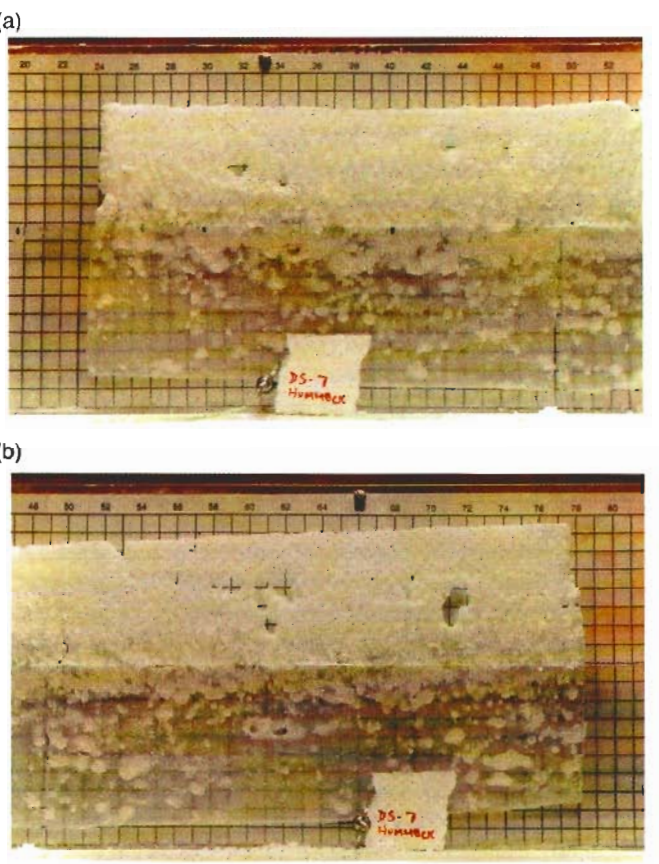

Fig. 8-11. The bubbly upper ice layers at DS-7. Each photograph is actually a juxtaposition of separate photographs of each of two distinct layers comprising the upper 8.5 cm of the ice. (a) and (b) show distinct samples taken at the site.

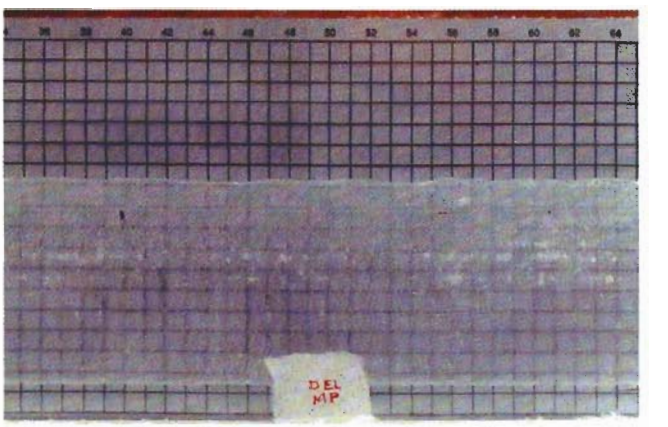

Fig. 8-12. A thick section of the upper layers of the Del Norte melt pond. Unlike Figure 8-11, this is not a composite but rather a single photo. Note the distinct layer of bubbles within the ice.

single layer.) The ice is clear and nearly bubble-free except for a thin, sparse layer of well-defined bubbles a few centimeters below the snow–ice interface. Onstott reports snow–ice interface roughness parameters of $h = 0.8 \pm 0.03$ cm and $L = 2.8 \pm 1.9$ cm, thicknesses of 3.2 ± 0.3 cm for the clear upper layer of ice and 2 cm for the bubbly layer, and a mean bubble diameter in the bubbly layer of 1.3 mm.

Figure 8-13 presents a schematic ice morphology and quantitative salinity and density profiles for this site, again based on Gow's analysis of a core sample. In this case, the ice density is high enough to obtain reliable parameter estimates from the core throughout its length. The upper 12 cm of ice is slightly bubbly with a bulk density of 0.875 g/cm^3, and ice below this layer is columnar. Total ice thickness was also greater than 1.5 m at this site; here again, we expect no effect of the lower ice boundary or seawater on signatures. Figure 8-13 also includes Grenfell's observations of parameters in a thin, light snow layer overlying the melt pond. Grenfell reports air, air–snow interface and snow–ice interface temperatures of –17, –16, and –11°C, respectively, with an estimated error in this case of ±1°C.

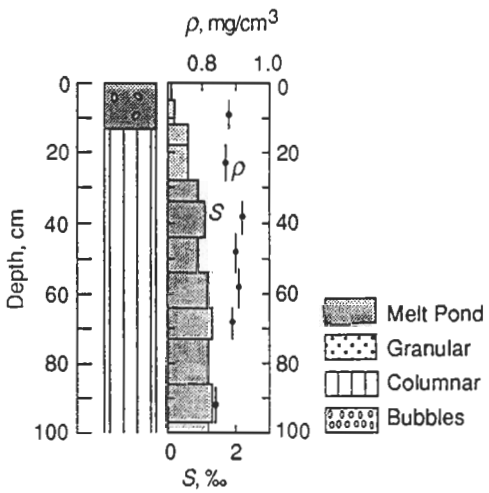

Snow: Layer Thickness = 8 cm
Consists of Platelets and Rimed Needles
Platelets 0.1 mm Thick and 0.5 mm Wide
Needles 0.1 to 0.2 mm Thick and 0.3 to 0.6 mm Long
Snow Density Approximately 0.1 gm/cm^3

Ice: Has a 12-cm Frozen Pond Layer that is Slightly Bubbly Over Columnar Ice Below

Density Profile		Salinity Profile	
cm	gm/cm^3	cm	‰
0–15	0.875	0–5	0.1
15–30	0.87	5–13	0.2
30–43	0.92	13–28	0.6
43–54	0.90	28–34	0.9
54–64	0.91	34–44	1.1
64–73	0.89	44–54	0.9
		54–64	1.2
		64–73	1.3
		73–86	1.2
		86–97	1.3
		97–100	1.2

Fig. 8-13. Structure, density and salinity in the upper ice layers at the Del Norte melt pond, numerical density and salinity profiles and snow cover observations.

8.4.2 *Model Comparisons*

8.4.2.1. Independent Rayleigh scattering layers—physical optics. Application of this model at both sites is based on a physical model consisting of two bubbly ice layers overlain by dry snow. Volume scattering in the snow is negligible; the snow thus acts only as a layer of intermediate permittivity between the air above and ice below. This slightly increases transmission into the ice and reduces scattering at the snow–ice interface. Only the reduction in surface scattering has a noticeable effect in backscattering. Since this model does not compute emission, this is the sole effect of the snow layer in this section. Air bubbles in the two ice layers are modeled as Rayleigh-scattering spheres with a distribution of radii. Because we have no independent estimates of bubble size distributions, assumptions are made to fix the form of the bubble size distribution input to the scattering model. The form of the distribution is Gaussian with sharp truncations; the standard deviation is set arbitrarily at 50% of the mean radius and the resulting distribution is truncated on both sides at two standard deviations from the mean. The mean radius varies between sites and between layers at each site.

The characterization data indicate minimal salinity in the upper ice layers. The relative permittivity of ice between bubbles is therefore set at 3.14 + i0.01, for all sites and all layers. As noted in Section 8.2.2.2, an effective permittivity for each bubbly ice layer is then computed according to a Polder–van Santen type formula and the measured layer density. The air bubbles are assumed to reside in an effective background medium with this effective permittivity for purposes of computing their scattering cross sections. Thus a given bubble scatters less, according to this model, when situated in a low-density ice layer than in a higher density layer because the effective dielectric contrast is lower in the latter case.

Layer thicknesses in the model are set equal to the measured mean layer thicknesses. Rough surface scattering is assumed negligible except at the air–snow and snow–ice interfaces; only scattering at the snow–ice interface significantly affects results at incidence angles greater than 20°. Roughness statistics for this latter interface are also drawn directly from the characterization measurements.

Figure 8-14(a) compares multipolarization observations with computed, HH-polarized backscattering cross sections

at 10 GHz for the site DS-7 (recall that the model does not compute cross-polarized backscattering, and that its predictions for like-polarization differ chiefly when surface scattering is significant). According to the model, backscattering at this site is dominated by volume scattering from the two bubbly ice layers; surface scattering is insignificant for incidence angles between 20 and 60°. The lower, denser, bubbly layer at DS-7 contributes most of the volume scattering in this model. This results because the permittivity of bubbles in the lower layer contrasts more strongly with the density-dependent effective background permittivity than in the lower density layer above. The predominant model sensitivity is therefore to parameters in the lower ice layer. Figure 8-14(a) shows results computed using three mean bubble diameters (but holding bulk density constant) in the lower layer. The bubble diameter of 4 mm in the lower layer is the mean diameter measured independently. Mean bubble diameter in the upper layer was set at 4.5 mm. The results span a range of approximately 3 dB for a 50% variation in mean bubble size (and, by way of the assumptions in the physical model, the same variation in the width of the size distribution). Results for the independently reported mean bubble size and for the smaller bubble size agree well with the HH-polarized observations.

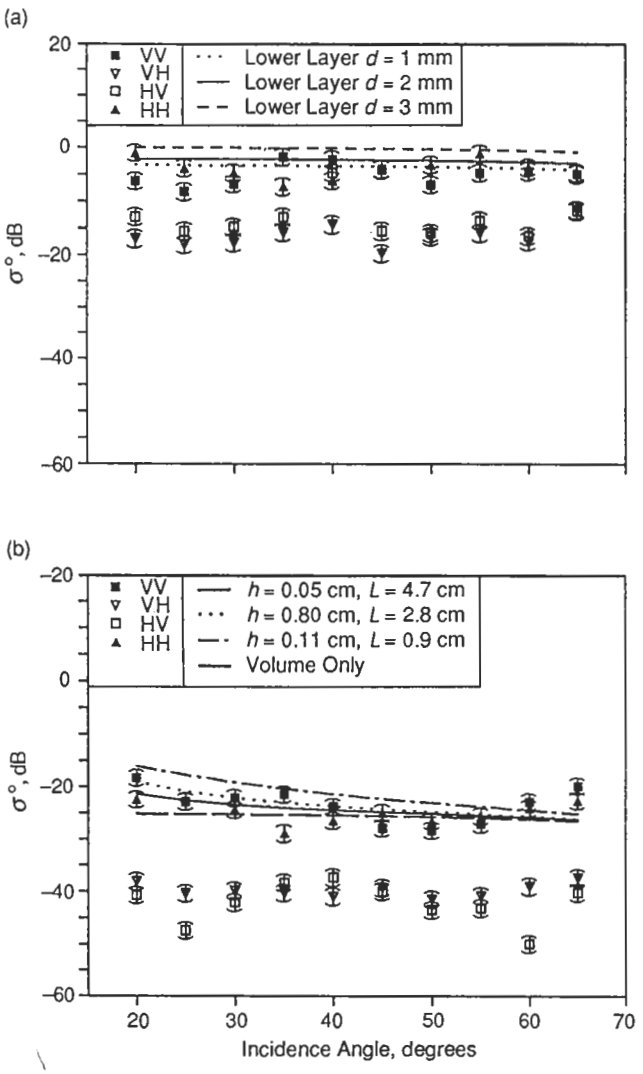

Fig. 8-14. Comparison of 10-GHz backscattering observations from DS-7 and the Del Norte melt pond with model predictions based on the independent Rayleigh scattering layer model of Section 8.2.2.2 for like-polarized backscattering cross sections at 10 GHz at (a) DS-7 for different assumed bubble sizes in the lower scatter layer, and (b) the Del Norte melt pond.

Model results also compare well with observations at the melt pond site. Figure 8-14(b) shows four model curves for the 10 GHz, HH-polarized backscattering cross section as a function of incidence angle. The four curves at this site show the effects of different assumptions for snow–ice interface roughness. The lowest curve results from volume scattering alone (from the thin layer of bubbles within the melt pond), and falls approximately 2–5 dB below the observations. The upper three curves correspond to the smoothest, most probable, and roughest surfaces consistent with independent characterization. The middle curve, corresponding to the most probable roughness parameters, agrees notably well with the observations. Note that these curves are for HH-polarization; computed VV-polarization curves are similar but slightly lower at incidence angles less than 35°, where surface scattering plays some role (Sections 8.2.2.2 and 8.3.2.2).

8.4.2.2. Dense medium radiative transfer. The application of DMRT to this case is based on an ice model of two scattering layers overlying a homogeneous, nonscattering basement. The (scalar) permittivity of the basement is computed from the equations of Frankenstein and Garner [1967] and Vant et al. [1978] for moderately saline ice (3‰) at a temperature of –9°C, consistent with the characterization information. DMRT presently assumes planar layer interfaces; the snow–ice interface roughness is therefore neglected. The dry snow layer reported in the characterization data has at most a negligible effect on backscattering, though perhaps not on emission. A two-layer DMRT model for emission is presently under development but is not fully operational as of this writing. The DMRT results presented here are therefore limited to backscattering and this in turn permits neglect of the snow layer.

The densities in each layer, which determine the total volume fractions occupied by scatterers, are set equal to the independently measured layer densities. The scatterers in each layer are assumed spherical, Rayleigh-scattering air bubbles embedded in a background of ice. Because the characterization data specify only mean bubble size, it is desirable to employ a plausible single-parameter distribution of bubble radii in the ice model. A truncated Rayleigh distribution is employed in this case. (Note that use of a Rayleigh distribution is separate from the Rayleigh-scattering assumption.) The mode of the distribution is set equal to the reported mean bubble radius; this fixes the

width of the distribution as well. The largest bubbles in the distribution are relatively few, but they scatter strongly because Rayleigh scattering increases rapidly with increasing particle size. If appreciable numbers of bubbles are present that because of their size act as Mie rather than Rayleigh scatterers, the total amount of scattering may be seriously overpredicted. The Rayleigh size distribution in this model is therefore truncated at an upper value of bubble diameter for which Rayleigh scattering remains a reasonable approximation, at least in view of the relative abundance and fraction of total scattering from bubbles near this size.

Figures 8-15(a) and (b) show computed backscattering cross sections at 10 GHz for site DS-7, based on densities in the upper and lower ice layers of 0.457 g/cm^3 and 0.728 g/cm^3, respectively, and upper and lower layer bubble mode diameters of 2.5 mm and 2 mm, respectively (the latter diameter was set at the reported mean void diameter for the lower layer—the assumed size distribution then includes substantial numbers of bubbles with the mean reported bubble size). The salinity of the background ice is taken to be 0‰. The curves in Figure 8-15(a) result from using a cutoff of 2 cm diameter in the bubble size distribution, while those in Figure 8-15(b) result from a cutoff of 0.96 cm. The former cutoff is a slightly liberal size limit for the Rayleigh size distribution (in our experience), whereas the latter cutoff is a slightly conservative limit. The like-polarization results in Figure 8-15(a) agree well with the observations, except perhaps at incidence angles greater than 55° where the observations seem to show a nonphysical upturn. The cross-polarized cross sections from DMRT, however, seem approximately 4 to 5 dB higher than those observed. Adopting the more conservative upper limit on bubble sizes, Figure 8-15(b), leads to like-polarized results approximately 1 to 3 dB lower than observed while the corresponding cross-polarized results agree with the data very closely.

Figure 8-15(c) shows corresponding results for the Del Norte melt pond. The physical model in this case consists of a 2 cm thick layer containing bubbles with mode diameter 1.3 mm, overlain by a 3.2 cm thick layer containing very small bubbles (mode diameter 0.1 mm). The bubble sizes in this case are small enough to make cutoffs unnecessary. The density of both layers is 0.87 g/cm^3, and the relative permittivity of background ice is set in this case to 3.2 + i0.02 to reflect the slight ice salinity reported at this site. Model results agree with the like-polarized observations to within 3 dB or less for angles between 25° and 55°. The upturn in the observations at 20° is probably due to rough surface scattering, but this model indicates that the dominant mechanism in the observed return at larger angles remains volume scattering. Note, however, that the DMRT cross-polarized predictions at this site fall approximately 10 dB below the observations.

The strongest input parameter sensitivities in this model are to mean (or mode) bubble size. For size distributions other than Rayleigh, parameters controlling the relative

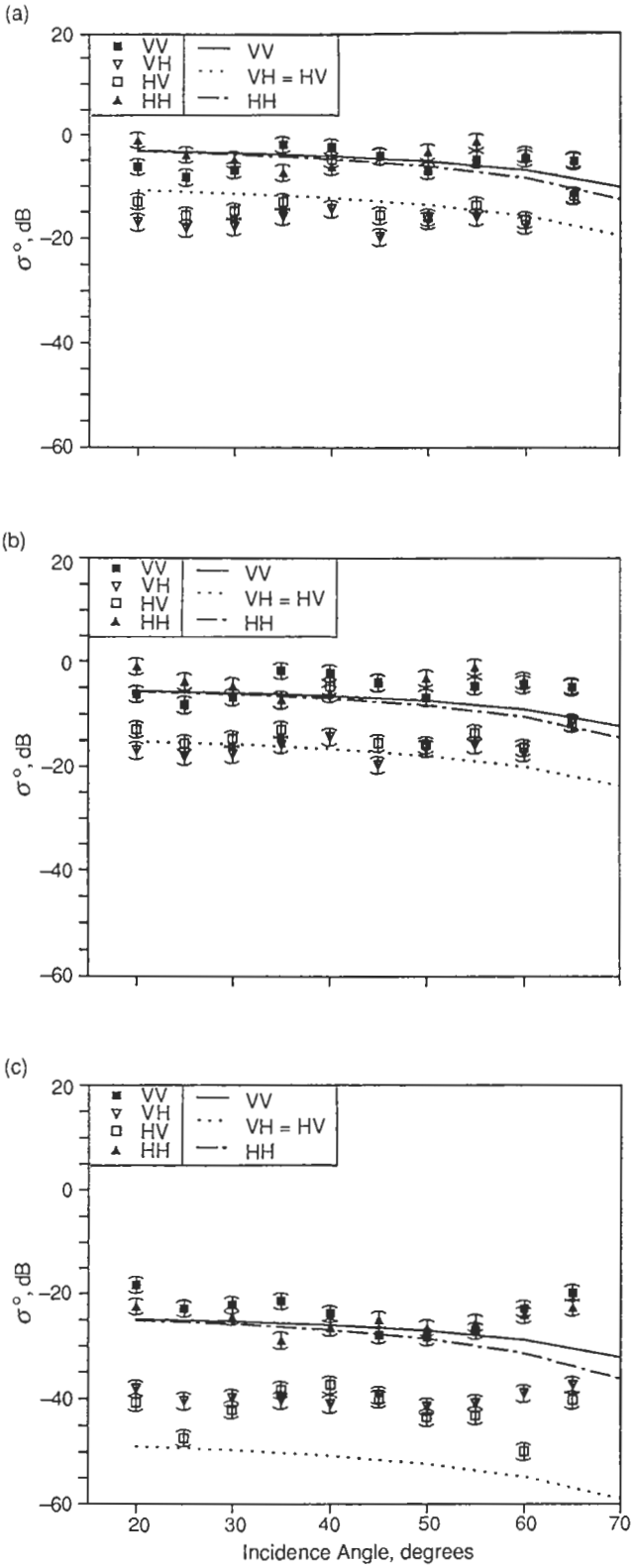

Fig. 8-15. Comparison of 10 GHz backscattering observations from DS-7 and the Del Norte melt pond with model predictions based on Dense Medium Radiative Transfer theory. Backscattering cross sections at 10 GHz at DS-7 for (a) 2-cm and (b) 0.90-cm truncations of the bubble size distribution in the lower bubbly layer, and (c) like-polarized backscattering cross sections at 10 GHz at the Del Norte melt pond.

abundance of larger radius particles are also sensitive model inputs. For example, varying the mode diameter of bubble sizes between approximately 1.1 and 1.5 mm in the bubbly melt pond layer above causes the VV-polarized cross section to vary by approximately 7 dB and the cross-polarized cross section to vary by 12 dB. A smaller sensitivity to salinity (i.e., to the imaginary part of the background ice permittivity), and much smaller sensitivities to layer thickness and density are also present in the model.

It is interesting that the independent scattering model in Section 8.4.2.1 predicts less volume scattering for the Del Norte melt pond site than does DMRT. This may seem contrary to our earlier statement that, for given input parameters, DMRT predicts less scattering than independent scattering. However, the physical models of this section and the last differ in their bubble size distributions, effective extinction coefficients, and other parameters. The large bubbles in the Rayleigh size distribution scatter disproportionately to their abundance, raising the level of scattering in the DMRT model. The independent scattering model includes a nonclassical decrease in scattering with decreasing ice density due to its decreased dielectric contrast between each bubble and the background ice. Thus the comparison between these two models is not simple. Comparison of DMRT and the model of Section 8.4.2.1 over a range of densities would give a clearer picture of the differences between them.

8.4.2.3. Dense medium theory—integral equation method. The physical model assumed in DMT-IEM presently includes only a single scattering layer. Thus application of DMT-IEM to the DS-7 and Del Norte sites requires the derivation of effective parameters for single scattering layers from the characterization data.

At DS-7, the physical model for the ice consists of an 8-cm thick layer of low-salinity ice (relative permittivity 3.3 + i0.003) containing single-sized, spherical, air bubbles of diameter 4 mm. The volume fraction of air bubbles is 40%. The relative permittivity of the underlying ice is the same as the effective permittivity of the bubbly ice, 2.2 + i0.01. Both the upper (snow–ice) and lower (ice–ice) interfaces are assumed rough with roughness parameters $h = 0.14$ cm, $L = 2.0$ cm. The snow layer is neglected. Model results for like-polarized, 10 GHz backscattering cross sections, shown in Figure 8-16(a), agree with observations to within approximately 3 dB for incidence angles less than 55°. Cross-polarized backscattering is not computed. The model predicts that volume scattering completely dominates rough surface scattering at DS-7 for incidence angles greater than 30°. Accordingly, the most sensitive model input parameter in this case is mean bubble size.

At the melt pond site, the physical model consists of a 6-cm thick layer containing single-sized, 1.5 mm diameter air bubbles; the air bubbles occupy 5% of the layer volume. The relative permittivities of the background ice and ice under the layer are both 3.1 + i0.01. The snow layer is again neglected, and identical roughnesses for the snow–ice and ice–ice interfaces are again assumed, with parameters $h = 0.11$ cm, $L = 4.3$ cm. Figure 8-16(b) shows the resulting cross sections and comparison with observations; agreement is again good. At this site, DMT-IEM indicates a more important role for scattering from the snow–ice interface (because the permittivities of the ice layer background and underlying ice match, scattering from the lower layer interface is negligible).

It may seem puzzling that a model which predicts more scattering than independent scattering agrees approximately as well with like-polarized observations as do DMRT (which predicts less scattering than independent scattering) and the independent scattering model of Section 8.2.2.2. Note that the physical model used by DMT assumes a single bubble size set at the independently estimated mean size,

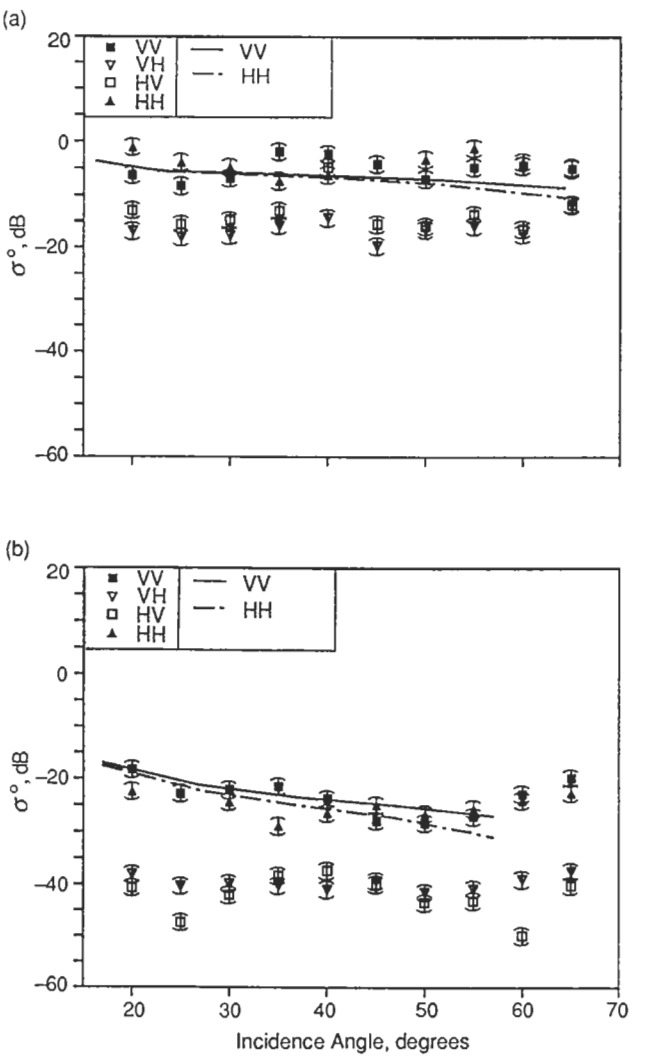

Fig. 8-16. Comparison of 10 GHz backscattering observations from DS-7 and the Del Norte melt pond with model predictions based on the Dense Medium Theory—Integral Equation Method. (a) Backscattering cross sections at 10 GHz at DS-7, and (b) like-polarized backscattering cross sections at 10 GHz at the Del Norte melt pond.

whereas DMRT and the independent scattering model both assume size distributions with significant numbers of bubbles larger than the mean size. The larger bubbles scatter out of proportion to their relative abundance in the size wavelength (i.e., Rayleigh scattering) regime in this case study. Thus, DMT predicts roughly the same level of backscattering as the other two models, because it predicts greater scattering from smaller bubbles and does not assume the presence of larger bubbles.

8.4.2.4. Many layer strong fluctuation theory. The physical model for ice built into many layer SFT (bubbles only on the boundaries of 1 cm diameter ice crystals) makes treatment of ice like that in Figure 8-10 problematic; the assumptions connecting ice salinity, density, and so on to permittivity correlation functions seem unsuited to ice so different from congelation ice. The application of many layer SFT to site DS-7 therefore treats the upper, very low density ice layers as layers of relatively large, spherical ice particles embedded in air. Beneath the 10-cm, low-density snow layer, the model employs a snow-like layer of density 0.460 g/cm^3 consisting of 5-mm diameter ice particles. Beneath this is a second layer of 3-mm diameter ice particles with density 0.728 g/cm^3. Underlying these layers is high-density congelation ice with salinities given by those in the measured profile. A model snow cover with parameters set at the independently estimated values covers the ice. Figure 8-17(a) shows the computed effective emissivities for DS-7 as functions of frequency at incidence angle 50°. The model results roughly reproduce the drop in emissivities between 6.7 and 18.7 GHz, but then rise again with increasing frequency, contrary to observations. The relatively good agreement between the model and observations at 18.7 GHz carries over at all incidence angles, Figure 8-17(b). Computed like-polarized backscattering cross sections at 10 GHz, Figure 8-17(c), are also in good agreement with observation, but predicted cross polarized cross sections are well below the observations.

The situation is somewhat improved for the melt pond site. The physical model for the ice at this site is more nearly suited to the assumptions about ice morphology in many layer SFT. The melt pond site is modeled as very low salinity congelation ice with 1.2 mm diameter bubbles. The number density of bubbles is determined by bulk density, for each of five layers within the upper 54 cm of ice. Layer densities and salinities are set directly from the measured profiles. Figure 8-18 compares the results with observations. The 50° emissivity spectrum, Figure 8-18(a), compares well with observations at 18.7 and 37 GHz, though disagreements arise at 90 GHz and especially at the lower frequencies. The angular emissivity responses at 18.7 and 37 GHz, Figures 8-18(b) and (c), also agree reasonably well with observation, though the H-polarized emissivities oscillate as functions of angle due to coherent interactions from various ice layers to a greater degree than do the observations. The model is quite sensitive to details of the salinity

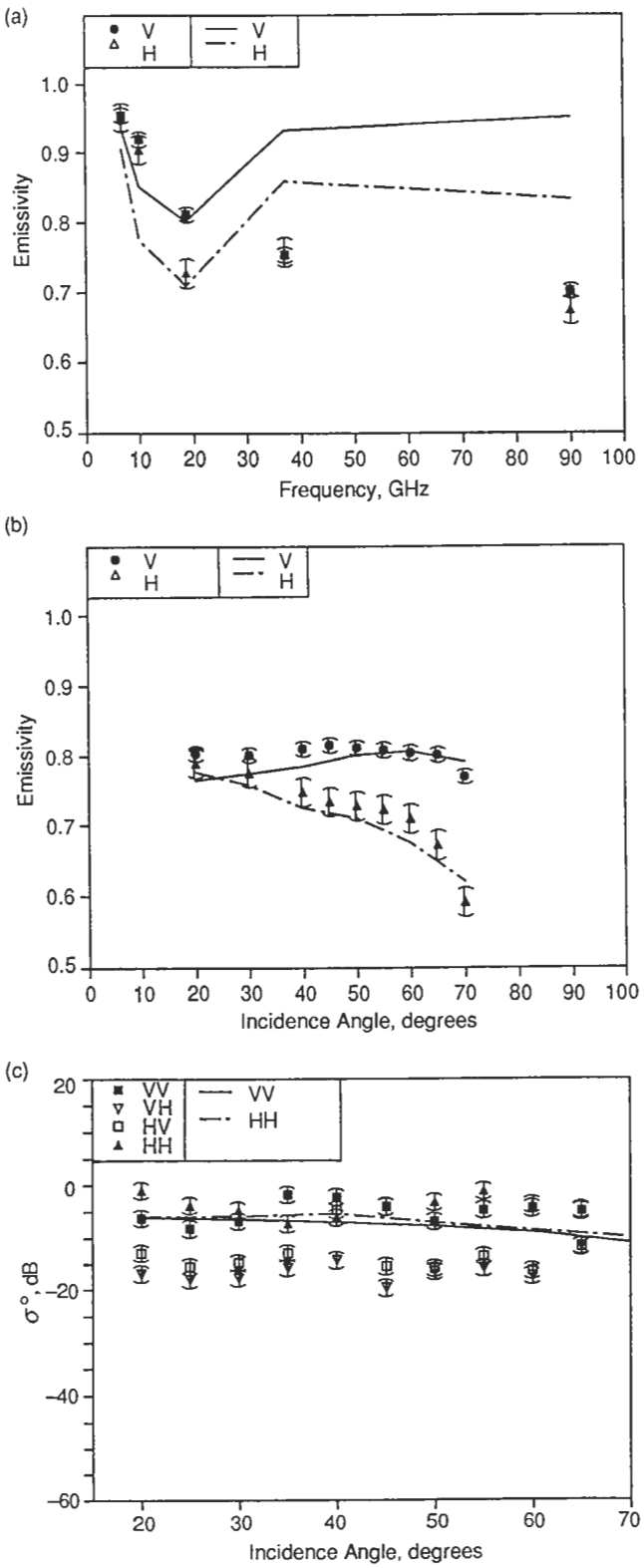

Fig. 8-17. Comparison of observations with emissivities and 10 GHz backscattering cross sections computed using the many layer SFT model for DS-7. (a) Emissivity versus frequency at an incidence angle of 50°; (b) emissivity versus incidence angle at 18.7 GHz; and (c) backscattering cross sections versus incidence angle at 10 GHz.

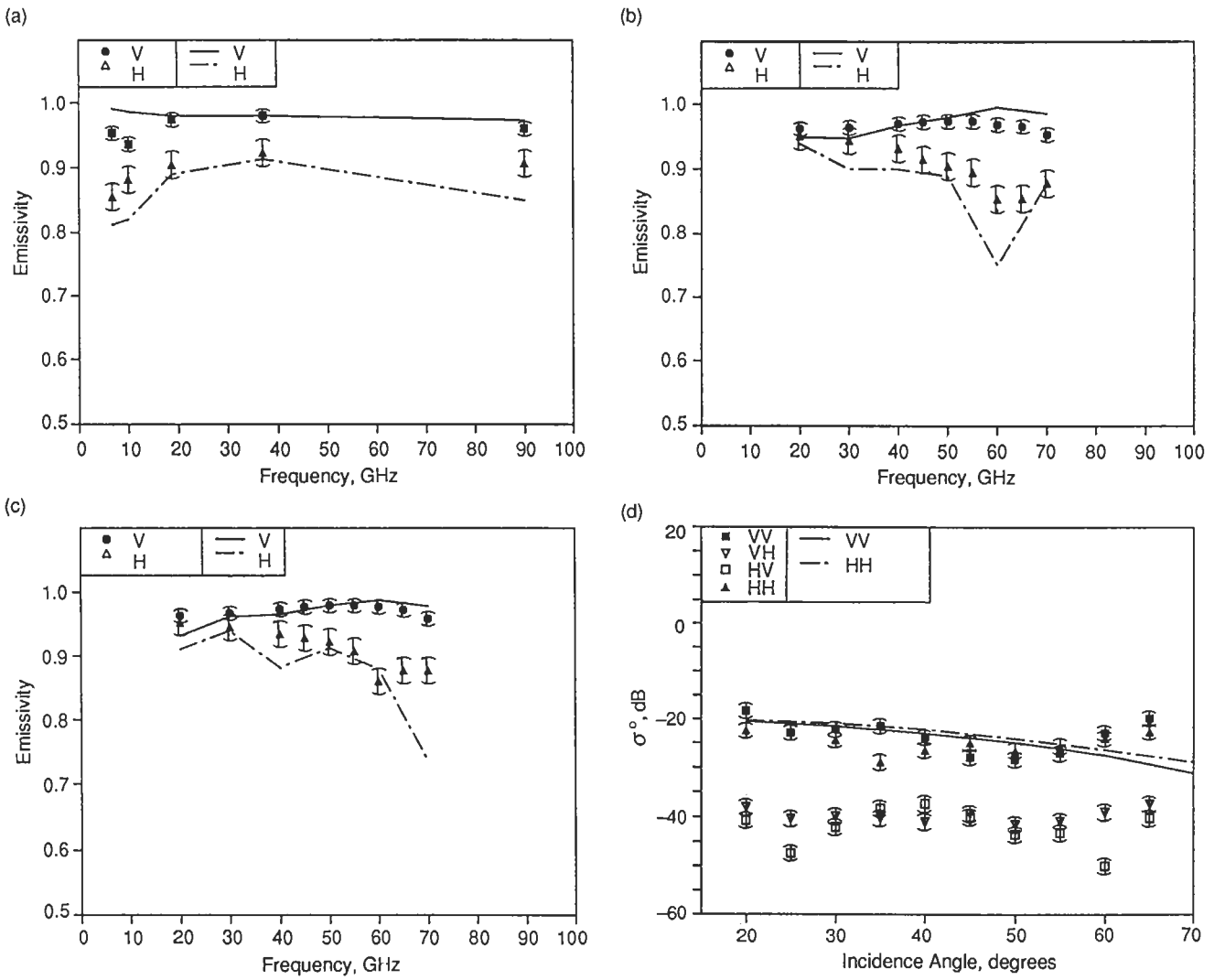

Fig. 8-18. Comparison of observations with emissivities and 10 GHz backscattering cross sections computed using the many layer SFT model for the Del Norte melt pond. (a) Emissivity versus frequency at an incidence angle of 50°; (b) emissivity versus frequency at 18.7 GHz; (c) emissivity versus frequency at 37 GHz; and (d) backscattering cross sections versus incidence angle at 10 GHz.

profile and the snow depth, suggesting that coherent effects may be overstated in the model. Note that the model has accurately tracked the change in like-polarized backscattering cross sections between DS-7 and the melt pond, Figure 8-18(d).

8.4.2.5. Modified radiative transfer. The physical model for MRT in this case consists of a uniform, infinitely thick scattering layer with a slight amount of azimuthal anisotropy, i.e., with a preferred direction tilted slightly off vertical and oriented in a particular way relative to the radar look direction. This physical model results in cross-polarized backscattering even with the current, first-order solution of MRT.

The dielectric parameters for site DS-7 are mean relative permittivities of 2.0 + i0.001 and 2.1 + i0.002 in directions orthogonal to and parallel to the preferred direction, respectively. The preferred direction is tilted 4° from vertical and oriented 45° from the radar/radiometer look direction. The normalized variances of permittivity are 0.2 and 0.25 in the orthogonal and parallel directions, respectively; the corresponding permittivity correlation lengths are 2 mm and 2.5 mm, respectively. These parameters lead to the results in Figures 8-19(a) and (b) for backscattering and emission. Like- and cross-polarized backscattering fall 7 dB or more below observations for most angles, while computed emissivities show both levels and trends at variance with observation.

Dielectric parameters for the melt pond site are set at 2.8 + i 0.004 and 2.9 + i0.005 for orthogonal and parallel mean permittivities, respectively. Normalized variances are 0.17 orthogonal and 0.20 parallel; permittivity correlation

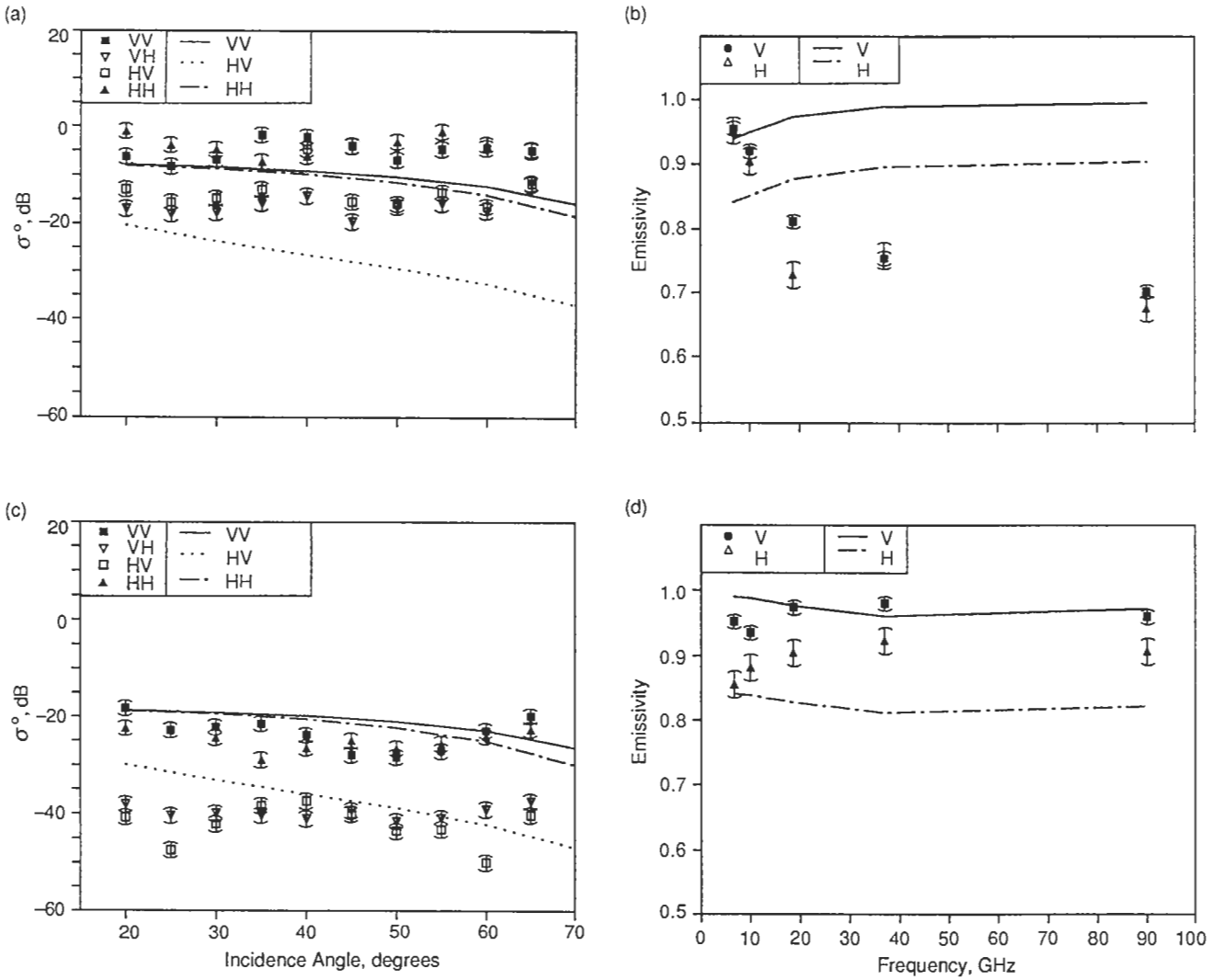

Fig. 8-19. Comparison of observations with emissivities and 10 GHz backscattering cross sections computed using Modified Radiative Transfer for DS-7 and the Del Norte melt pond. (a) 10-GHz backscattering cross sections versus incidence angle at DS-7; (b) emissivity versus frequency at an incidence angle of 50° at DS-7; (c) 10-GHz backscattering cross sections versus incidence angle at the Del Norte melt pond; and (d) emissivity versus frequency at an incidence angle of 50° at the Del Norte melt pond.

lengths are 0.3 and 0.4 mm orthogonal and parallel, respectively. The orientation of the preferred direction is the same as for site DS-7. Figures 8-19(c) and (d) show the results for backscattering and emission. Backscattering cross sections are generally above the data while computed emissivities show much more polarization difference than is observed.

Model sensitivity is again greatest for variations in permittivity correlation lengths. For small tilts of the preferred direction, such as that employed here, neither scattering cross sections nor emissivities show strong sensitivities to the azimuthal orientation. Additional model sensitivity information is provided by Lee and Mudaliar [1988] and Mudaliar and Lee [1990].

8.4.3 Discussion

DS-7 appears to be the opposite extreme to the gray ice in our first case study, not only in terms of ice age, but also of its strength as a scatterer. Though only two of the models we apply treat emission, both of these predict strong scattering effects in both backscattering and emission. Four of the models produce backscattering results that agree with like-polarized observations to within 3 dB at DS-7, and volume scattering is the dominant scattering mechanism according to all four. This is encouraging, and may be surprising given the difficulty of describing real ice at DS-7 in the physically idealized terms required by the models. However, the four models offer considerably different accounts of the physics behind the signatures. Clearly,

differing assumptions about the physical model for the scattering medium and approximations in scattering physics can combine to produce results that are indistinguishable at a given single frequency, especially in the absence of bubble size distribution information. We expect that stringent multifrequency, multipolarization tests including characterization of bubble size distributions would distinguish which of the accounts is closer to reality. The strong scattering situation evidently makes accurate computation of emissivities difficult; neither of the models we applied at this site accurately explained passive observations.

Backscattering cross sections for the Del Norte melt pond are comparable to those of the gray ice in our first case study, though they fall off less rapidly with increasing incidence angle and show less polarization dependence. The melt pond surface has larger height variations but smaller surface slopes than the gray ice; of course the melt pond also has lower salinity and larger volume scatterers. Two of the models we apply at the Del Norte site indicate that rough surface scattering and volume scattering both contribute significantly to 10 GHz backscattering in the midrange of incidence angles. DMRT and many layer SFT account successfully for like-polarized backscattering in terms of volume scattering alone for incidence angles greater than 30°. The cross-polarization results from DMRT are lower than observations, but model sensitivities are such that a minor change in mean bubble size could bring them into near agreement. Again, the four models differ substantially in their accounts of the volume scattering physics behind the observations, but they agree that volume scattering is an essential part of backscattering from even a dense melt pond. Together with the DS-7 results, this indicates that volume scattering from bubbles is the predominant backscattering mechanism for nearly all old ice at 10 GHz.

The effect of scattering on emission from melt ponds remains unclear. Many layer SFT predicted accurate like-polarized cross sections based on volume scattering alone, but 19 and 37 GHz emissivities from this model showed an oversensitivity to depth variation in model parameters. This suggests the possibility that scattering at these two frequencies is weak enough for reflectivity to again control emissivity at this site. Emission calculations using DMRT and DMT-IEM, which were not available at the time of this writing but should soon be possible, should help in understanding this issue.

8.5 CONCLUSIONS

We set out in this chapter to clarify the state-of-the-art in ice signature modeling. To this end, our case studies have yielded several pertinent results.

We are able to compute emissivities for our smooth, bare gray ice sample accurate to within less than 0.05 for frequencies of 19 and 37 GHz and incidence angles less than 55°. This statement is based on results from several models, including polarimetric SFT, many layer SFT, and Modified Radiative Transfer. Ice 8 cm thick was, in our example, effectively infinitely thick at 19 and 37 GHz. The essential physics according to each of these models is the connection between the emission and the reflectivity properties of the ice, and thus the mean dielectric properties of the upper few centimeters of ice; emission from this ice type was modified only minimally by scattering. More accurate emissivity calculations for this ice will therefore depend on improved treatment of near-surface dielectric variations; note, however, that this conclusion may not hold for the type of strongly scattering gray ice reported in some radar observations (Chapters 5 and 14). At 6.7 and 10 GHz, we observe a distinct feature in the frequency dependence of emission. Emissivities computed using the many layer SFT model agree with observations to within 0.04. According to this model, the essential signature physics is coherent interaction between waves from various depths in the ice; the interaction is modulated by ice thickness and differing salinity profiles (i.e., differing growth histories). This frequency-dependent emissivity feature may prove valuable in sensing gray ice thickness from aircraft (or from spacecraft if the spatial resolution of radiometers can be improved sufficiently), provided we can learn to interpret the signatures correctly. The present model ignores thickness variations with the sensor footprint, however, and may overestimate signature sensitivity to frost flower and surface brine layers; this requires further investigation.

Backscattering from our gray ice sample at 10 GHz may be explicable in terms of scattering from the rough air–ice interface alone, but support for this explanation from our comparison is not strong. Conventional first-order perturbation theory correctly predicts the difference between like-polarized backscattering cross sections, but the cross sections themselves fall only barely within the estimated range of uncertainty below the observations. Uncertainty in surface roughness characterization may play a role. However, scattering from the air–ice interface alone is clearly insufficient to explain the observed backscattering level at 5 GHz. Neither did volume scattering models in our study reproduce the polarization and incidence angle dependencies observed for gray ice backscattering. The Dense Medium Model—Integral Equation Method provides a close fit to both 5 and 10 GHz like-polarized backscattering observations based on scattering from roughness at an abrupt ice–water interface in addition to the air–ice interface. All our models indicate considerable 5 GHz penetration to the lower part of an 8 cm gray ice sheet, making this explanation plausible. However, we unfortunately have no quantitative characterization data for the lower ice surface with which to test it. There are other presently plausible mechanisms which also cannot be ruled out on the basis of our data. Such mechanisms may figure in the anomalous brightness of some gray ice in 5 and 10 GHz SAR images (Chapter 5). On the other hand, the results of Ulander et al. [1992] indicate that scattering from the air–ice interface may indeed dominate 5 GHz backscattering from thicker first-year ice. The operational importance of 5 GHz SAR's

for sea ice observation strongly motivates further investigation of these issues.

Four of our models computed 10 GHz, like-polarized cross sections for raised, bubbly old ice and for a melt pond that agree with observations to within 3 dB, using input parameters reasonably derived from independent ice characterization. One model (DMRT) also produced cross-polarized cross sections that agree with observations to within 5 dB at the bubbly ice site. The strongest input parameter sensitivities in each model are to bubble size parameters, but the natural variability in ice density is so large that it drives the cross section variation between sites in our study. A quantitative link between cross sections and density suggests that the variance of cross sections in an old floe is perhaps (or perhaps not, see below) related to the variance of ice density on the floe. The latter variance is evidently related to refrozen melt pond coverage, a parameter of geophysical interest. Thus, our results suggest a possible avenue of inquiry for remote sensing development. However, the four models otherwise offer considerably different accounts of the relevant scattering physics. Our data are presently not sufficient to determine which version is closer to reality. In contrast to backscattering, we find emission at the strongly scattering site difficult to model. This finding, together with our gray ice results, suggests that perhaps backscattering is more easily computed when scattering is very strong while accurate emission computations are more feasible when scattering is weak.

Several caveats are worth considering when applying our results or reasoning from them. First, our case studies examine only individual examples of three broad types of sea ice, and there exist few other such case studies in the literature. Moreover, we were compelled to focus on small areas of ice that could be characterized sufficiently to support our model comparison. We can say little about the ranges of natural variability for each type, and we cannot rule out the possibility that any given example constitutes an extreme within the range for its type. Pending replication, our results should therefore be considered provisional. Second, our case studies address only two relatively simple kinds of sea ice in a menagerie of ice types and conditions. Our work cannot support sweeping generalizations about scattering mechanisms in broad ice types or our present signature modeling abilities for those types. Finally, our comments on model sensitivities may or may not bear on signature variability for a given ice type when scattering dominates the signature. Present signature models compute a mean signature, i.e., a signature averaged over random medium realizations drawn from a single ensemble (with given means and variances of ice properties). Changing input parameters amounts to choosing a different ensemble, not just a different realization; thus, examining the mean signature variation for varying input parameters may not give an accurate picture of signature variance for different realizations drawn from the same ensemble.

Based on our study (and its limitations), we can draw a few conclusions about the state of microwave sea ice signature modeling and new work that would contribute to remote sensing. We now possess models to treat a variety of potentially significant effects and processes. However, the sophistication of our models exceeds our sophistication in knowing which model to apply when and why. Fundamental questions remain as to which effects must be treated to compute specified signatures for specified ice types and conditions. This problem can be addressed by further studies like those of Ulander et al. [1992] and ours covering a wider range of ice types and conditions. Good ice and snow characterization is central to this effort, and improved methods of estimating parameters, especially scatterer size distributions and ice surface roughness, are sorely needed. Further studies are more likely to edify than confuse if they begin with simpler conditions and move toward the more complex. To benefit remote sensing more immediately, the selected cases must also involve ice types and situations that play significant geophysical roles.

However, there is a gap between focussed studies at points on the ice and interpretation of data from airborne and spaceborne sensors. The spatial resolution of these sensors is typically larger than the areas we can characterize intensively enough for rigorous model tests. We presently know little about the magnitudes and length scales of inherent, natural variability in ice properties, either those that control signatures or, in some cases, those of geophysical significance. Lacking this understanding, it is problematic to link mean signatures for a small but sufficiently characterized ice region with signatures measured by sensors that average over some (perhaps much) larger area. This is, at the very least, a key validation problem for any signature model or remote sensing algorithm. It requires that we work out sampling strategies for characterization measurements both within single sensor resolution cells and for sufficient numbers of cells within a swath or scene. Sampling strategies must be based on better information about the horizontal length scales of both ice and signature variabilities as well as signature model sensitivities. The Canadian Sea Ice Monitoring Site (SIMS) experiment [Barber et al., 1991] is a valuable effort in this direction.

Better information alone might suffice if the problem were one of validation alone, but this may not always be the case. In virtually all signature models, we envision a slab of ice that is homogeneous, at least in a statistical sense, in the horizontal. If the sensor footprint covers an inhomogeneous area of ice, we assume, often only implicitly, that the actual ice can be replaced by some homogeneous slab, the signature of which we compute using model inputs derived from actual ice parameters. In remote sensing, we equate the signature we measure with that of the slab and, using a link between slab properties and slab signatures, infer some effective geophysical parameter for the actual, horizontally inhomogeneous ice. We assume the effective parameter has some simple relation (usually equality) to the actual geophysical parameter, appropriately averaged over the footprint. These are significant assumptions. Our guidelines as to when they may break down

are mostly intuitive. Failure of these assumptions could fundamentally limit retrieval of some geophysical parameters; ways might also be found of exploiting such a failure. The issues here bear at least a superficial similarity to validation and parameterization problems in large- or mesoscale geophysical models; the relevant physical processes there often occur on scales much smaller than the model grid size (see, for example, Wettlaufer [1991]). In any case, a quantitative description of this process seems possible and should be undertaken. The problem is also amenable to ground-based experimental investigation; this work could begin modestly and might involve only analyzing existing data in a new way.

Finally, the benefits of signature modeling have so far scarcely reached operational sea ice remote sensing. We have made little use of the expanded information inherent in time series of observations, but this avenue looks very promising (Chapter 24). It is essential that we begin developing methods to estimate geophysical sea ice parameters based on what we understand now. Initial algorithms are likely to be limited in applicability and less accurate than may be desired, but a starting place is necessary before refinements can begin. Moreover, even imperfect results may show unexpected and valuable spatial or temporal patterns in geophysical variables; this is precisely the situation, for example, in the remote sensing of sea surface winds using microwave scatterometry [Freilich and Chelton, 1986]. The key thing is to begin. As we enter an era of routine floods of remote sensing data, the value of physical signature models in geophysical data interpretation must be made manifest.

REFERENCES

Arcone, S. A., A. J. Gow, and S. McGrew, Structure and dielectric properties at 4.8 and 9.5 GHz of saline ice, *Journal of Geophysical Research, 91(C12)*, pp. 14,281–14,303, 1986.

Attema, E. P. W. and F. T. Ulaby, Vegetation modelled as a water cloud, *Radio Science, 13*, pp. 357–364, 1978.

Barber, D. G., D. D. Johnson, and E. F. LeDrew, Measuring climatic state variables from SAR images of sea ice: The SIMS SAR validation site in Lancaster Sound, *Arctic, 44, Supplement 1*, pp. 108–121, 1991.

Blinn, J. C., III, J. E. Conel, and J. G. Quade, Microwave emission from geological materials: Observations of interference effects, *Journal of Geophysical Research, 77*, pp. 4366–4378, 1972.

Bogorodskii, V. V. and G. P. Khokhlov, Anisotropy of the microwave dielectric constant and absorption of Arctic drift ice, *Soviet Phys.–Tech. Phys., 22(6)*, pp. 747–749, 1977.

Bredow, J. W. and S. P. Gogineni, Comparison of measurements and theory for bare and snow-covered saline ice, *IEEE Transactions on Geoscience and Remote Sensing, GE-28(4)*, pp. 456–463, 1990.

Chen, K. S. and A. K. Fung, An iterative approach to surface scattering simulation, *Proceedings of the 1990 International Geoscience and Remote Sensing Symposium*, pp. 405–408, European Space Agency, University of Maryland, College Park, Maryland, 1990.

Chen, M. F., K. S. Chen, and A. K. Fung, A study of the validity of the integral equation model by moment method simulation—cylindrical case, *Remote Sensing of the Environment, 29(3)*, pp. 217–228, 1989.

Dashen, R. and D. Wurmser, Approximate representations of the scattering amplitude, *Journal of Mathematical Physics, 32(4)*, pp. 986–996, 1991.

Davis, R. E., J. Dozier, and A. T. C. Chang, Snow property measurements correlative to microwave emission at 35 GHz, *IEEE Transactions on Geoscience and Remote Sensing, GE-25(6)*, pp. 751–757, 1987.

Drinkwater, M. R., *Radar Altimetric Studies of Polar Ice*, Ph.D. dissertation, Scott Polar Research Institute, University of Cambridge, Cambridge, England, 231 pp., 1987.

Drinkwater, M. R., LIMEX'87 ice surface characteristics: Implications for C-band SAR backscatter signatures, *IEEE Transactions on Geoscience and Remote Sensing, GE-27(5)*, pp. 501–513, 1989.

Drinkwater, M. R. and G. B. Crocker, Modelling changes in the dielectric and scattering properties of young snow-covered sea ice at GHz frequencies, *Journal of Glaciology, 34(118)*, pp. 274–282, 1988.

Eom, H. J., *Theoretical Scatter and Emission Models for Microwave Remote Sensing*, Ph.D. dissertation, University of Kansas, Lawrence, Kansas, 1982.

Frankenstein, G. and R. Garner, Equations for determining the brine volume of sea ice from –0.5 to –22.9°C, *Journal of Glaciology, 6*, pp. 943–944, 1967.

Freilich, M. H. and D. B. Chelton, Wavenumber spectra of pacific winds measured by the Seasat scatterometer, *Journal of Physical Oceanography, 16*, pp. 741–757, 1986.

Fung, A. K. and H. J. Eom, Application of a combined rough surface and volume scattering theory to sea ice and snow backscatter, *IEEE Transactions on Geoscience and Remote Sensing, GE-20(4)*, pp. 528–536, 1982.

Fung, A. K. and H. J. Eom, A study of backscattering and emission from closely packed inhomogeneous media, *IEEE Transactions on Geoscience and Remote Sensing, GE-23(5)*, pp. 761–767, 1985.

Fung, A. K. and G. W. Pan, A scattering model for perfectly conducting random surfaces: I. Model development, *International Journal of Remote Sensing, 8(11)*, pp. 1579–1593, 1987a.

Fung, A. K. and G. W. Pan, A scattering model for perfectly conducting random surfaces: II. Range of validity, *International Journal of Remote Sensing, 8(11)*, pp. 1594–1605, 1987b.

Fung, A. K., Z. Li, and K. S. Chen, Backscattering from a randomly rough dielectric surface, *IEEE Transactions on Geoscience and Remote Sensing*, in press, 1991.

Golden, K. M. and S. F. Ackley, Modeling of anisotropic electromagnetic reflection from sea ice, *Journal of Geophysical Research, 86(C9)*, pp. 8107–8116, 1981.

Grenfell, T. C., Surface-based passive microwave studies of multiyear sea ice, *Journal of Geophysical Research, 97(C3), pp.* 3485–3501, 1992.

Ishimaru, A., *Wave Propagation and Scattering in Random Media*, Academic Press, New York, 1978.

Ishimaru, A., J. S. Chen, P. Phu, and K. Yoshitomi, Numerical, analytical, and experimental studies of scattering from very rough surfaces and backscattering enchancement, *Waves in Random Media, 1*, pp. S91–S107, 1991.

Jackson, D. R., D. P. Winebrenner, and A. Ishimaru, Comparison of perturbation theories for rough-surface scattering, Journal of the Acoustical *Society of America, 83(3)*, pp. 961–969, 1988.

Jin, Y.–Q. and J. A. Kong, Strong fluctuation theory for scattering, attenuation and transmission of microwaves through snowfall, *IEEE Transactions on Geoscience and Remote Sensing, GE-23(5)*, pp. 754–760, 1985.

Jin, Y.–Q. and M. Lax, Backscattering enhancement from a randomly rough surface, *Physical Review B, 42(16)*, pp. 9819–9829, 1990.

Kim, Y.–S., R. G. Onstott, and R. K. Moore, The effect of a snow cover on microwave backscatter from sea ice, *IEEE Journal of Oceanic Engineering, OE-9(5)*, pp. 383–388, 1984a.

Kim, Y.–S., R. K. Moore, and R. G. Onstott, *Theoretical and Experimental Study of Radar Backscatter From Sea Ice*, Remote Sensing Laboratory Technical Report 331-37, University of Kansas, Lawrence, Kansas, 1984b.

Kim, Y.–S., R. K. Moore, R. G. Onstott, and S. P. Gogineni, Towards identification of optimum radar parameters for sea-ice monitoring, *Journal of Glaciology, 31(109)*, pp. 214–219, 1985.

Lee, J. K. and J. A. Kong, Active microwave remote sensing of an anisotropic random medium layer, *IEEE Transactions on Geoscience and Remote Sensing, GE-23(6)*, pp. 910–923, 1985a.

Lee, J. K. and J. A. Kong, Electromagnetic wave scattering in a two-layer anisotropic random medium, *Journal of the Optical Society of America, A2(12), pp.* 2171–2186, 1985b.

Lee, J. K. and J. A. Kong, Modified radiative transfer theory for a two-layer anisotropic random medium, *Journal of Electromagnetic Waves and Applications, 2(3/4)*, pp. 391–424, 1988.

Lee, J. K. and S. Mudaliar, Backscattering coefficients of a half-space anisotropic random medium by the multiple scattering theory, *Radio Science, 23(3)*, pp. 429–442, 1988.

Lin, F. C., J. A. Kong, R. T. Shin, A. J. Gow, and S. A. Arcone, Correlation function study for sea ice, *Journal of Geophysical Research, 93(C11)*, pp. 14,055–14,063, 1988.

Livingstone, C. E. and M. R. Drinkwater, Springtime C-band SAR backscatter signatures of Labrador Sea marginal ice: Measurements versus modelling predictions, *IEEE Transactions on Geoscience and Remote Sensing, GE-29(1)*, pp. 29–41, 1991. (Correction, *IEEE Transactions on Geoscience and Remote Sensing, 29(3)*, p. 472, 1991.)

Mudaliar, S. and J. K. Lee, Microwave scattering and emission from a half-space anisotropic random medium, *Radio Science, 25(6)*, pp. 1199–1210, 1990.

Nghiem, S., *The Electromagnetic Wave Model for Polarimetric Remote Sensing of Geophysical Media*, Ph.D. dissertation, Massachusetts Institute of Technology, Cambridge, Massachusetts , 1991.

Perovich, D. K. and A. J. Gow, A statistical description of the microstructure of young sea ice, *Journal of Geophysical Research, 96(C9)*, pp. 16,943–16,953, 1991.

Reber, B., C. Mätzler, and E. Schanda, Microwave signatures of snow crusts: Modelling and measurements, *International Journal of Remote Sensing, 8(11)*, pp. 1649–1665, 1987.

Rice, S. O., Reflections of electromagnetic waves from slightly rough surfaces, *Commun. Pure Appl. Math. 4*, pp. 351–378, 1951.

Sackinger, W. M. and R. C. Byrd, *Reflection of Millimeter Waves From Snow and Sea Ice*, IAEE Report 7203, Institute of Arctic Environmental Engineering, University of Alaska, Fairbanks, Alaska, January 1972.

Stogryn, A., The bilocal approximation for the electric field in strong fluctuation theory, *IEEE Transactions on Antennas and Propagation, AP-31(6)*, pp. 985–986, 1983a.

Stogryn, A., A note on the singular part of the dyadic Green's function in strong fluctuation theory, *Radio Science, 18(6)*, pp. 1283–1286, 1983b.

Stogryn, A., Correlation functions for random granular media in strong fluctuation theory, *IEEE Transactions on Geoscience and Remote Sensing, GE-22(2)*, pp. 150–154, 1984a.

Stogryn, A., The bilocal approximation for the effective dielectric constant of an isotropic random medium, *IEEE Transactions on Antennas and Propagation, AP-32(5)*, pp. 517–520, 1984b.

Stogryn, A., Strong fluctuation theory for moist granular media, *IEEE Transactions on Geoscience and Remote Sensing, GE-23(2)*, pp. 78–83, 1985.

Stogryn, A., A study of the microwave brightness temperature of snow from the point of view of strong fluctuation theory, *IEEE Transactions on Geoscience and Remote Sensing, GE-24(2)*, pp. 220–231, 1986.

Stogryn, A., An analysis of the tensor dielectric constant of sea ice at microwave frequencies, *IEEE Transactions on Geoscience and Remote Sensing, GE-25(2)*, pp. 147–158, 1987.

Stogryn, A. and G. J. Desargent, The dielectric properties of brine in sea ice at microwave frequencies, *IEEE Transactions on Antennas and Propagation, AP-33(5)*, pp. 523–532, 1985.

Thorsos, E., The validity of the Kirchhoff approximation for rough surface scattering using a Gaussian roughness spectrum, *Journal of the Acoustical Society of America, 83*, pp. 78–92, 1988.

Thorsos, E. and D. R. Jackson, Studies of scattering theory using numerical methods, *Waves in Random Media, 3*, pp. S165–S190, 1991.

Tsang, L., Passive remote sensing of dense nontenuous media, *Journal of Electromagnetic Waves and Applications, 1(2)*, pp. 159–173, 1987.

Tsang, L., Dense medium radiative transfer theory for dense discrete random media with particles of multiple sizes and permittivities, Chapter 5, *Progress in Electromagnetic Research, 6,* edited by A. Priou, Elsevier, New York, 1991.

Tsang, L. and A. Ishimaru, Radiative wave equations for vector electromagnetic propagation in dense nontenuous media, *Journal of Electromagnetic Waves and Applications, 1(1)*, pp. 59–72, 1987.

Tsang, L. and J. A. Kong, Microwave remote sensing of a two-layer random medium, *IEEE Transactions on Antennas and Propagation, AP-24(3)*, pp. 283–288, 1976.

Tsang, L. and J. A. Kong, Scattering of electromagnetic waves from random media with strong permittivity fluctuations, *Radio Science, 16*, pp. 303–320, 1981.

Tsang, L., J. A. Kong, and R. T. Shin, *Theory of Microwave Remote Sensing*, John Wiley and Sons, New York, 1985.

Tucker, W. B., III, A. J. Gow, and J. A. Richter, On small-scale horizontal variations in salinity in first-year sea ice, *Journal of Geophysical Research, 89(C4)*, pp. 6505–6514, 1984.

Ulaby, F. T., R. K. Moore, and A. K. Fung, *Microwave Remote Sensing—Active and Passive, Vol. II: Radar Remote Sensing and Surface Scattering and Emission Theory*, Addison–Wesley Publishing Company, Reading, Massachusetts, 1982.

Ulander, L. M. H., R. Johansson, and J. Askne, C-band radar backscatter of Baltic Sea ice, *International Journal of Remote Sensing,* in press, 1992.

Vallese, F. and J. A. Kong, Correlation function studies for snow and ice, *Journal of Applied Physics, 52(8)*, pp. 4921–4925, 1981.

Vant, M. R., R. O. Ramseier, and V. Makios, The complex dielectric constant of sea ice at frequencies in the range 0.1–40 GHz, *Journal of Applied Physics, 49(3)*, pp. 1264–1280, 1978.

Vedernikova, E. A. and M. V. Kabanov, Scattering of optical radiation by a system of closely spaced scatterers, *Optical Spectroscopy, 37(1)*, 1974.

Wen, B., L. Tsang, D. P. Winebrenner, and A. Ishimaru, Dense medium radiative transfer theory: Comparison with experiment and application to microwave remote sensing and polarimetry, *IEEE Transactions on Geoscience and Remote Sensing, 28(1)*, pp. 46–59, 1990.

Wettlaufer, J., Heat flux at the ice–ocean interface, *Journal of Geophysical Research, 96(C4)*, pp. 7215–7236, 1991.

Winebrenner, D. P., L. Tsang, B. Wen, and R. West, Sea-ice characterization measurements needed for testing of microwave remote sensing models, *IEEE Journal of Oceanic Engineering, 14(2)*, pp. 149–158, 1989.

Yueh, S. H., J. A. Kong and R. T. Shin, Scattering from randomly oriented scatterers with strong permittivity fluctuations, *Journal of Electromagnetic Waves and Applications, 4(10)*, pp. 983–1004, 1990.

Zuniga, M. A. and J. A. Kong, Modified radiative transfer theory for a two-layer random medium, *Journal of Applied Physics, 51(10)*, pp. 5228–5244, 1980.